

1 **Measuring NDC80 binding reveals the molecular basis of tension-dependent**
2 **kinetochore-microtubule attachments**

3

4 **AUTHORS:** Tae Yeon Yoo^{1,*}, Jeong-Mo Choi², Che-Hang Yu³, Rohit V. Pappu², and Daniel J.
5 Needleman^{1,3}

6

7 **AFFILIATIONS:**

8 ¹Department of Molecular and Cellular Biology and Faculty of Arts and Sciences Center for Systems
9 Biology, Harvard University, Cambridge, MA 02138, USA

10 ²Department of Biomedical Engineering and Center for Biological Systems Engineering, Washington
11 University in St. Louis, St. Louis, MO 63130, USA

12 ³John A. Paulson School of Engineering and Applied Sciences, Harvard University, Cambridge, MA
13 02138, USA.

14 *Correspondence: tyoo@fas.harvard.edu

15

16 **Abstract:** Proper kinetochore-microtubule attachments, mediated by the NDC80 complex, are required
17 for error-free chromosome segregation. Erroneous attachments are corrected by the tension dependence of
18 kinetochore-microtubule interactions. It has been difficult to establish the molecular basis of this process
19 because of the lack of techniques to quantify NDC80 binding in vivo. Here, we present a method, based
20 on fluorescence lifetime imaging microscopy and Förster resonance energy transfer, to quantitatively
21 measure the fraction of NDC80 complexes bound to microtubules at individual kinetochores in living
22 human cells. We found that NDC80 binding is modulated in a chromosome autonomous fashion over
23 prometaphase and metaphase, and is predominantly regulated by centromere tension. We show that the
24 tension dependency of NDC80 binding requires the proper localization of Aurora B kinase, which
25 modulates NDC80 binding. Our results lead to a mathematical model of the molecular basis of tension-

1 dependent NDC80 binding to kinetochore microtubules in vivo.

2

3 **INTRODUCTION**

4 Chromosome segregation errors lead to aneuploidy and micronuclei formation, which are closely
5 associated with cancer, infertility, and birth defects (Santaguida and Amon, 2015). Accurate chromosome
6 segregation is believed to result from a process that actively suppresses potential errors. The mechanism
7 of error correction remains unclear, but extensive evidence suggests that it is based on the regulation of
8 the attachment of microtubules to chromosome via the kinetochore, a protein complex assembled at
9 centromeres (Godek et al., 2015). Previous works suggested that error correction is largely due to the
10 detachment of kinetochore microtubules (kMTs) being regulated by the tension across centromeres,
11 which selectively destabilizes erroneous kMT attachments bearing low tension and stabilizes proper
12 attachments under high tension (Nicklas and Ward, 1994, Liu et al., 2009, Akiyoshi et al., 2010, Lampson
13 and Cheeseman, 2011, Godek et al., 2015). However, the molecular mechanism of the tension-dependent
14 regulation of kMT attachments is still poorly understood.

15 The highly conserved NDC80 complex is the major coupler of the kinetochore to microtubules
16 (Cheeseman et al., 2006, DeLuca et al., 2006). In human mitotic cells, ~250 NDC80 complexes are
17 recruited at the outer layer of each kinetochore (Suzuki et al., 2015) and interact with ~20 kMTs by
18 directly binding to them (Cheeseman and Desai, 2008, Maiato et al., 2004, Rieder, 1982). In vitro
19 experiments showed that the binding affinity of NDC80 for microtubules decreases upon the
20 phosphorylation of the N-terminal tail of Ndc80/Hec1 protein by Aurora B kinase (Cheeseman et al.,
21 2006, Zaytsev et al., 2014, Zaytsev et al., 2015), which may explain the contribution of Aurora B to error
22 correction (Tanaka et al., 2002). It is unclear how the biochemical activities of NDC80 and Aurora B
23 result in tension-dependent kMT detachment. The lack of techniques to measure the binding of the
24 NDC80 to kMTs in vivo has been a major obstacle to investigate this.

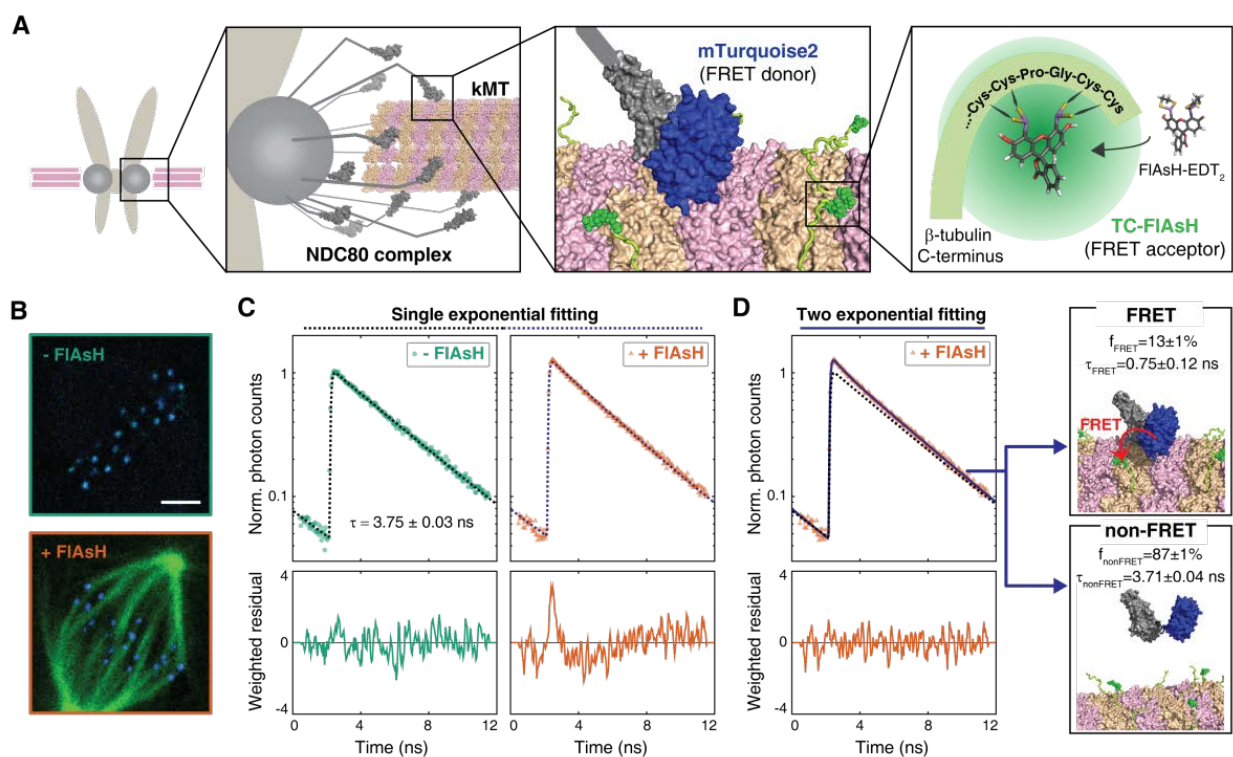
25

1 **RESULTS**

2 **FLIM-FRET measures the fraction of donor-labeled NDC80 complexes engaged in FRET with** 3 **acceptor-labeled microtubules**

4 Inspired by previous work (Posch et al., 2010), we sought to develop a Förster Resonance Energy
5 Transfer (FRET) based approach to directly measure the association between the NDC80 complex and
6 kinetochore microtubules (kMTs) in living cells. We engineered U2OS cells stably expressing Nuf2, a
7 subunit of the NDC80 complex, N-terminally labeled with a cyan fluorescent protein, mTurquoise2
8 (Figure 1A). In this same cell line, we also inserted a tetracysteine (TC) motif at the C-terminus of β -
9 tubulin (TUBB) using CRISPR-induced homologous recombination, which becomes fluorescent after
10 binding to the membrane-permeable dye FAsH (Hoffmann et al., 2005) (Figure 1A and B). The small
11 size (six amino acids) of the TC motif minimizes the negative effects of labeling the C-terminus of
12 tubulin, allowing the engineered cells to pass successfully through mitosis (Andresen et al., 2004).
13 CRISPR-mediated endogenous tubulin tagging ensures low cell-to-cell variation and a high fraction of
14 labeled β -tubulin, which was estimated to be $26.1\% \pm 5.4\%$ (SD) (see Supplemental experiments in
15 Methods).

16 We used time-correlated single photon counting (TCSPC) fluorescence lifetime imaging
17 microscopy (FLIM) to quantitatively measure the FRET between mTurquoise2 and TC-FAsH in tissue
18 culture cells (Figure S1). TCSPC FLIM-FRET provides fluorescence decay curves of the donor
19 fluorophore at each pixel location. If the donor fluorophore has a single-exponential fluorescence decay
20 curve when not engaged in FRET, then when it is engaged in FRET the fluorescence decay curve will
21 also be single-exponential, but with a shorter lifetime. A pixel containing a mixture of such donor
22 fluorophores engaged in FRET and not engaged in FRET displays a fluorescence decay curve that is a
23 sum of two exponentials. Bayesian analysis of the fluorescence decay curves provides a bias-free
24 measurement of the relative fraction of the two exponentials, and hence the fraction of donor fluorophores
25 engaged in FRET (Yoo and Needleman, 2016, Kaye et al., 2017). In contrast to intensity-based FRET



1
2 **Figure 1. FLIM-FRET measurement of NDC80-kMT binding in human tissue culture cells.**
3 (A) Engineered U2OS cell expressing mTurquoise2-NDC80 and β -tubulin-TC-FIAsH. NDC80 (gray),
4 mTurquoise2 (blue) and TC-FIAsH (green).
5 (B) Two-photon microscopy images of the engineered U2OS cells not exposed to FIAsH (top) and
6 exposed to FIAsH (bottom). 3 μ m scale bar. mTurquoise2 (blue) and FIAsH (green).
7 (C) Example fluorescence decay curves of mTurquoise2-NDC80 in the engineered U2OS cells not
8 exposed to FIAsH (left, green circle) and exposed to FIAsH (right, orange triangle), plotted with the best-
9 fit single-exponential decay models (black and blue dotted lines). Corresponding weighted residuals (the
10 deviation of data from model) are plotted below after being smoothed to display systematic deviations.
11 (D) The fluorescence decay curve of mTurquoise2-NDC80 in the presence of FIAsH labeling (orange
12 triangle, same as (C)), plotted with the best-fit two-exponential model (blue solid line). The single-
13 exponential model fit to the fluorescence decay curve in the absence of FIAsH labeling (black dotted line)
14 plotted together for comparison. Corresponding smoothed weighted residual for the two-exponential
15 model is plotted below. Long- and short-lifetime exponentials correspond to the mTurquoise2-NDC80
16 populations in non-FRET state and FRET state, respectively, and their relative amplitudes give the
17 fraction of each population. To facilitate the comparison, the fluorescence decay curves in the absence
18 and presence of FIAsH labeling were normalized such that they asymptotically overlap.

1 methods, FLIM-FRET is capable of quantifying the fraction of donor fluorophores engaged in FRET
2 when donors and acceptors are differentially distributed in cells, and it is less prone to errors arising from
3 instrumental artefacts and photobleaching (Berezin and Achilefu, 2010).

4 We first characterized the fluorescence decay of mTurquoise2-NDC80 in the absence of FRET by
5 performing FLIM measurement on the engineered U2OS cells (mTurquoise2-NDC80/ β -tubulin-TC) that
6 were not exposed to FIAsh (Figure 1B, top). We found that their fluorescence decays are well described
7 as a single exponential with a lifetime of $3.75 \text{ ns} \pm 0.09 \text{ ns}$ (SD) (Figure 1C and S2A). As discussed above,
8 this single exponential decay profile is expected when the donor fluorophores do not engage in FRET. We
9 next measured the fluorescence decay of the mTurquoise2-NDC80 in the presence of FIAsh labeling of
10 microtubules. In this case, a single exponential provided a poor fit to the data, exhibiting significant
11 systematic deviations (Figure 1C). The fluorescence decay in the presence of FIAsh labeling was well fit
12 by a sum of two exponentials with lifetimes $3.71 \text{ ns} \pm 0.04 \text{ ns}$ (SE) and $0.75 \text{ ns} \pm 0.12 \text{ ns}$ (SE) (Figure 1D).
13 The long lifetime of the two-exponential fit was indistinguishable from the lifetime in the absence of
14 FRET ($p = 0.68$, two-sided Z-test), and thus corresponds to the non-FRET donor population. Therefore,
15 the short-lifetime species is the FRET donor population. The relative amplitude of the short- and long-
16 lifetime exponentials are 0.13 ± 0.01 (SE) and 0.87 ± 0.01 (SE), respectively, thus $13\% \pm 1\%$ (SE) of
17 donor fluorophores are engaged in FRET.

18

19 **FRET between mTurquoise2-NDC80 and FIAsh results from the NDC80-kMT binding**

20 Having demonstrated our ability to measure FRET between mTurquoise2-NDC80 and FIAsh in tissue
21 culture cells, we explored if the FRET is due to the binding of NDC80 to kMTs. We first engineered an
22 alternative construct with mTurquoise2 conjugated to the distally located C-terminus of Nuf2, far
23 removed from kMTs. This alternative construct displayed only a single long-lifetime state in either the
24 presence or absence of TC-FIAsh, arguing that FRET does not result from non-specific interactions
25 (Figure S2B, C and E). Incubating cells with nocodazole to depolymerize microtubules caused a reduction

1 of NDC80 FRET fraction from $13\% \pm 1\%$ (SE) to $3\% \pm 1\%$ (SE) (Figure S2D). Thus, FRET strongly
2 depends on the presence of microtubules.

3 We next investigated if NDC80 that is close to kMTs, but not bound to them, can lead to
4 appreciable FRET. Answering this requires knowing the Förster radius between mTurquoise2 and TC-
5 FIAsh, which we determined to be 5.90 ± 0.10 nm (SE) through a combination of FLIM measurements
6 and Monte Carlo simulations (see Figure S3 and Supplemental experiments in Methods). We next
7 performed large-scale Monte Carlo simulations of mTurquoise2-NDC80 at various distances from
8 FIAsh-labeled microtubules and simulated the fluorescence decay curves, which revealed that NDC80
9 more than 8 nm away from the kMT do not contribute to the short-lifetime FRET state (Figure S4A and
10 B). Thus, only NDC80 very close to the surface of kMTs contributes to FRET, consistent with FRET
11 resulting from NDC80 bound to kMTs, an interpretation further supported by biological perturbation
12 experiments described below.

13 Even though FRET results only from NDC80 bound to kMTs, the measured FRET fraction is not
14 identical to the fraction of NDC80 bound to kMTs because not all tubulin heterodimers are labeled with
15 TC-FIAsh. Using large scale Monte Carlo simulations of mTurquoise2-NDC80 bound to FIAsh-labeled
16 microtubules, we generated fluorescence decay curves for various NDC80 binding fractions, and
17 estimated the resulting NDC80 FRET fractions from a fit to a two-exponential decay (see Figure S4C and
18 Supplemental experiments in Methods). We found that the NDC80 FRET fraction increases linearly with
19 the NDC80 binding fraction with a slope of 0.42 ± 0.08 , indicating that 42% of attached mTurquoise2-
20 NDC80 contribute to the short-lifetime FRET state (Figure S4C). Thus, the measured FRET fraction of
21 13% in Figure 1D corresponds to 31% of NDC80 complexes being bound to kMTs.

22
23 **NDC80-kMT binding is regulated in a chromosome-autonomous fashion throughout prometaphase**

24 Using the FLIM-FRET measurements of NDC80-kMT binding, we first investigated how NDC80-kMT
25 binding evolves over the course of mitosis. We found that the average NDC80-kMT binding gradually

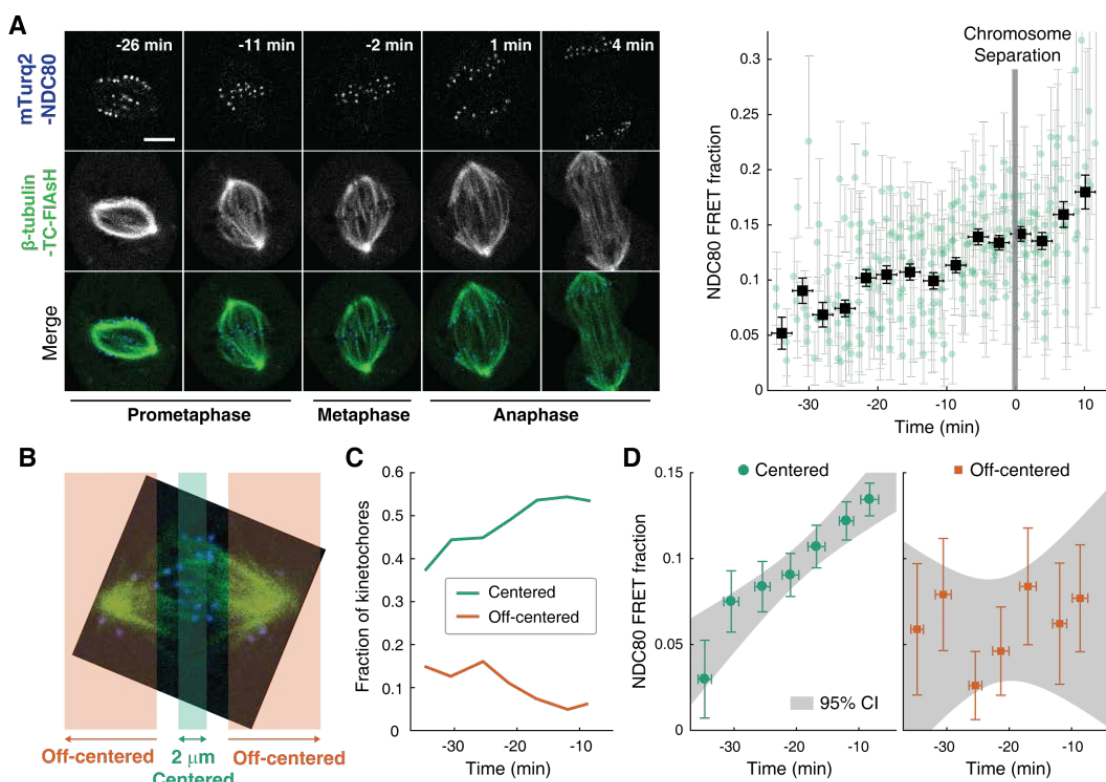
1 increases as mitosis progresses, with NDC80 FRET fraction rising from 7% in early prometaphase to 14%
2 in late metaphase, and reaching about 18% in anaphase (corresponding to NDC80 binding fractions of 17%
3 in prometaphase; 33% in late metaphase; and 43% in anaphase) (Figure 2A). This temporal change in
4 NDC80-kMT binding may underlie the previously observed decrease in kMT turnover throughout mitosis
5 (Kabeche and Compton, 2013, Zhai et al., 1995).

6 The change in the average NDC80-kMT binding over the course of error correction in prometaphase
7 could be due to a cell cycle-dependent coordinated regulation of NDC80 affinity across kinetochores
8 (coordinated regulation), an independent modulation of NDC80 on different chromosomes (chromosome-
9 autonomous regulation), or a combination of both. To investigate the contribution of chromosome-
10 autonomous regulation, we sought to determine if different populations of kinetochores in prometaphase
11 exhibit different NDC80-kMT binding. We compared the extent of the NDC80-kMT binding of
12 kinetochores centered at the metaphase plate to those located off-centered (Figure 2B), and found that the
13 centered kinetochores exhibit 2.0 ± 0.4 times higher NDC80 binding than the off-centered kinetochores.

14 We next investigated how the NDC80-kMT binding of centered and off-centered kinetochores change
15 with time in prometaphase. As mitosis progresses and the chromosomes align to the metaphase plate, the
16 number of kinetochores in the center region increases while the number of kinetochores in the off-center
17 region decreases (Figure 2C). NDC80-kMT binding continuously increases over time for the kinetochores
18 located in the center region, but remains constant with the FRET fraction of ~7% for the kinetochores in
19 the off-center region (Figure 2D). The observation of differences in NDC80 binding between different
20 subpopulations of kinetochores strongly argues for the existence of chromosome-autonomous regulation.

21 We speculate that the temporal increase in NDC80-kMT binding of centered kinetochores is due to the
22 gradual decrease in the number of kinetochores with erroneous attachment that transiently lie on the
23 metaphase plate. The constant NDC80-kMT binding of off-centered kinetochores argues for a lack of
24 temporal regulation of this subpopulation.

25



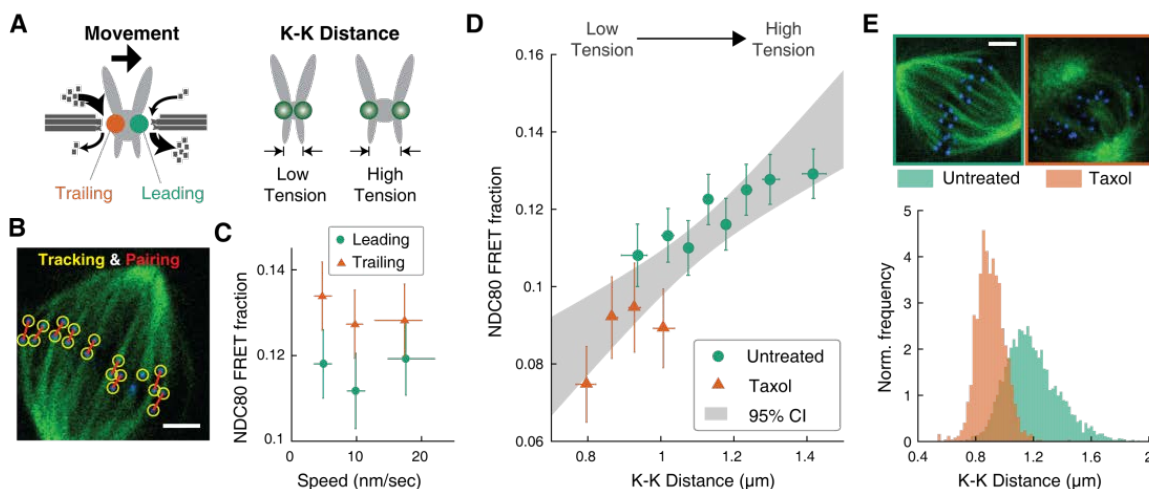
1
2 **Figure 2. NDC80-kMT binding is regulated in a chromosome-autonomous fashion.**
3 (A) Example cell images and time course of NDC80 FRET fraction from prometaphase to metaphase to
4 anaphase ($n = 12$ cells). Black squares are the mean, y-error bars are the SEM, and x-error bars are the SD
5 of the data points (green circles) in equally spaced time intervals. $5 \mu\text{m}$ scale bar.
6 (B) Kinetochore at each time point in prometaphase cells are divided into two groups, centered and off-
7 centered, based on their distances from the metaphase plate. Kinetochore less than $1 \mu\text{m}$ away from the
8 metaphase plate were classified as centered, and kinetochores more than $2.5 \mu\text{m}$ away were classified as
9 off-centered.
10 (C) Time course of the fraction of centered (green) and off-centered (orange) kinetochores in
11 prometaphase.
12 (D) Time course of NDC80 FRET fraction of centered (green circles) and off-centered (orange squares)
13 kinetochores in prometaphase ($n = 12$ cells, 2886 centered and 572 off-centered kinetochores). Data
14 points are the mean, y-error bars the SEM, and the x-error bars the SD in equally spaced time intervals.
15 Gray areas are the 95% confidence intervals for the linear fits.

1 **NDC80-kMT binding is dependent on centromere tension**

2 After demonstrating that different population of kinetochores exhibits different NDC80-kMT binding
3 throughout prometaphase, we next sought to investigate what factors contribute to chromosome-
4 autonomous regulation of the interaction between NDC80 and kMTs. Aligned chromosomes in U2OS
5 cells oscillate around the metaphase plate, with microtubules attached to the leading and trailing
6 kinetochores primarily depolymerizing and polymerizing, respectively (Tirnauer et al., 2002, Armond et
7 al., 2015) (Figure 3A). The distance between sister kinetochores (referred to as K-K distance) fluctuates
8 during the oscillation (Magidson et al., 2011), as the centromere deforms in response to the dynamic
9 change in tension (Figure 3A). Therefore, chromosome oscillation provides a window to study how
10 NDC80 binding is related to the kMT dynamics and centromere tension in a physiologically relevant
11 condition.

12 We first asked whether NDC80 binding is different on leading and trailing kinetochores. We acquired
13 time-lapse movies of 17 metaphase cells, tracked their kinetochores, identified sister kinetochores by their
14 relative motions (Figure 3B), and quantified the NDC80 binding fraction in groups of kinetochores with
15 similar velocities using FLIM-FRET analysis. We found that the NDC80 FRET fraction is higher at
16 trailing kinetochores ($12.8\% \pm 0.5\%$, SEM) than leading kinetochores ($11.4\% \pm 0.5\%$, SEM), regardless
17 of their speeds (Figure 3C), suggesting that NDC80 preferentially binds to polymerizing kMTs in vivo.
18 The preferential binding is statistically significant ($p < 0.02$, two-sided Z-test), yet small, presumably
19 because leading and trailing kinetochores have a mixture of both polymerizing and depolymerizing MTs
20 (Armond et al., 2015). This differential binding of NDC80 provides an explanation for the higher
21 detachment rate of depolymerizing microtubules from kinetochores in vitro (Akiyoshi et al., 2010).

22 The detachment rate of kMTs from kinetochores was shown to be reduced when tension was
23 increased using glass needles in classic micromanipulation experiments by Bruce Nicklas (Nicklas and
24 Koch, 1969). Since the NDC80 complex is the predominant coupler of the kinetochore to microtubules
25 (Cheeseman et al., 2006, DeLuca et al., 2006), we hypothesized that the tension-dependent detachment of



1
2 **Figure 3. NDC80-kMT binding is dependent on kMT dynamics and centromere tension.**
3 (A) (left) kMTs predominantly depolymerize at leading kinetochores and polymerize at trailing
4 kinetochores. (right) K-K distance is a proxy for centromere tension. Measuring NDC80-kMT binding
5 along with the kinetochore movement and K-K distance therefore reveals how NDC80-kMT binding is
6 related to the kMT dynamics and centromere tension.
7 (B) Image of a metaphase cell with mTurquoise2-NDC80 (blue) and β -tubulin-TC-FIAsH (green), and
8 kinetochore tracking (yellow circles) and pairing (red lines) results. 3 μ m scale bar.
9 (C) NDC80 FRET fraction vs. kinetochore speed for leading (green circle) and trailing (orange triangle)
10 kinetochores (n= 17 cells, 681 kinetochores/data point). Data points are the mean, y-error bars the SEM,
11 and the x-error bars the interquartile ranges within groups of kinetochores with similar velocities.
12 (D) NDC80 FRET fraction vs. K-K distance for untreated cells (green circle, n = 17 cells, 984
13 kinetochores/data point) and cells treated with 10 μ M taxol (orange triangle, n = 7 cells, 525
14 kinetochores/data point). Data points are the mean, y-error bars the SEM, and the x-error bars the
15 interquartile ranges within groups of kinetochores with similar K-K distances. Gray area is the 95%
16 confidence interval for the linear fit to the combined data.
17 (E) Histograms of K-K distances for the untreated (green) and taxol-treated (orange) cells. 3 μ m scale bar
18 in the cell images of mTurquoise2-NDC80 (blue) and beta-tubulin-TC-FIAsH (green).

1 kMTs results from tension-dependent NDC80-kMT binding. To test this possibility, we next investigated
2 the correlation between NDC80 FRET fraction and centromere tension, inferred by K-K distance, during
3 chromosome oscillations. We used FLIM-FRET analysis to measure the NDC80 binding in groups of
4 sister kinetochores with similar K-K distances, and observed a highly statistically significant positive
5 correlation ($p < 0.005$) between NDC80 FRET fraction and K-K distance (Figure 3D). We observed no
6 significant correlation between K-K distance and kinetochore velocity, arguing that NDC80 binding is
7 independently regulated by these two factors (Figure S5). In the absence of microtubules, the rest length
8 of K-K distance in human cell is $0.73 \mu\text{m} \pm 0.04 \mu\text{m}$ (Tauchman et al., 2015), significantly shorter than
9 the K-K distances during metaphase oscillations. Thus, in order to investigate a wider range of K-K
10 distance, we treated cells with taxol, which reduced K-K distances ($0.90 \mu\text{m} \pm 0.10 \mu\text{m}$, taxol vs. $1.19 \mu\text{m}$
11 $\pm 0.19 \mu\text{m}$, untreated, SD) (Figure 3E). Combining the data of untreated and taxol-treated cells, we found
12 that the NDC80 FRET fraction continually increases with K-K distance over the full range of K-K
13 distance (positive correlation, $p < 0.0005$) (Figure 3D). These observations suggest that NDC80-kMT
14 binding is dependent on the tension across the centromere. The extent of variation of NDC80-kMT
15 binding with K-K distance is comparable to the extent of variation over the course of mitosis, from
16 prometaphase to anaphase onset, as well as the extent of difference between centered and off-centered
17 kinetochores in late prometaphase (compare Figure 2D with 3A and D). Thus, the magnitude of the
18 tension-dependent regulation of NDC80-kMT binding is sufficient to account for the increase in NDC80-
19 kMT binding throughout prometaphase and metaphase. These results suggest that tension is a primary
20 regulator of NDC80-kMT binding during error correction.

21

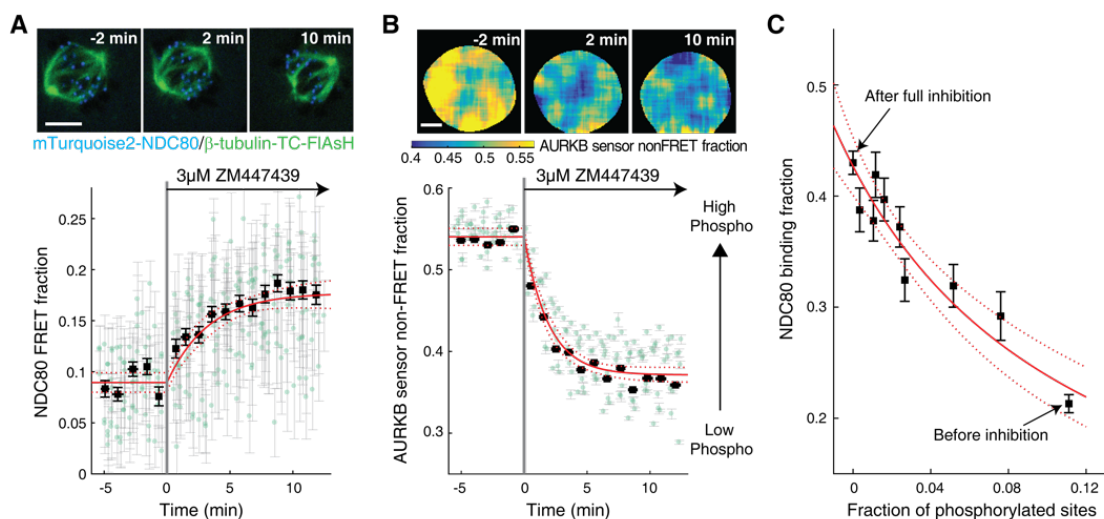
22 **Aurora B kinase regulates NDC80-kMT binding in a graded fashion in vivo**

23 Aurora B kinase is one of the best characterized components of the error correction process, and the N-
24 terminal tail of the Ndc80 protein in the NDC80 complex is a known substrate of Aurora B kinase that
25 contains nine phosphorylation sites (Tanaka et al., 2002, Biggins et al., 1999, Cheeseman et al., 2006,

1 DeLuca et al., 2006, Ciferri et al., 2008, Hauf et al., 2003). We used our FLIM-FRET technique to
2 investigate the relationship between Aurora B kinase activity and NDC80-kMT binding in cells. We first
3 added the ATP-competitive Aurora B inhibitor, ZM447439, to late prometaphase cells, and observed a
4 gradual increase in NDC80 FRET fraction over ~10 minutes, from 9% to nearly 18% (corresponding to
5 21% NDC80 binding fraction before Aurora B inhibition and 43% after the inhibition) (Figure 4A and
6 S6A). This result is consistent with previous in vitro biochemistry experiments that demonstrated that
7 Aurora B-mediated phosphorylation destabilizes NDC80-MT interactions (Cheeseman et al., 2006,
8 Zaytsev et al., 2014, Zaytsev et al., 2015).

9 We next sought to investigate how this inhibition influences Aurora B activity in cells. To do this,
10 we performed FLIM measurement on a cytoplasmic Aurora B FRET biosensor (Fuller et al., 2008), which
11 contains a kinesin-13 family Aurora B substrate whose phosphorylation obstructs intramolecular FRET
12 between mTurquoise2 and YPet (Figure S6B). During ZM447439 treatment, we found a continual
13 reduction in the fraction of the Aurora B sensors in the non-FRET state, a proxy for Aurora B
14 phosphorylation, from 0.540 ± 0.007 (SEM) to 0.368 ± 0.012 (SEM) (Figure 4B and S6C). Nuf2-targeted
15 Aurora B sensor responded to the ZM447439 treatment with similar kinetics, arguing that the time scale
16 of response to Aurora B inhibition is insensitive to the spatial location of the substrate (Figure S6D).

17 As the typical time scale of drug uptake is far slower than typical
18 phosphorylation/dephosphorylation kinetics (Thurber et al., 2014, Huang et al., 1997), it is reasonable to
19 assume that the phosphorylation level of Aurora B substrate is at steady state at each time point, so
20 plotting the measured NDC80 binding fraction (converted from FRET fraction) vs. phosphorylated level
21 (converted from Aurora B sensor non-FRET fraction) at each time point reveals their relationship. This
22 analysis showed a graded dependence of NDC80-kMT binding on phosphorylation (Figure 4C), which is
23 consistent with the relationship previously found between the number of aspartic acid phosphomimetic
24 mutations on truncated NDC80 constructs and their in vitro binding affinity to microtubules (Zaytsev et
25 al., 2014, Zaytsev et al., 2015). The increased NDC80-kMT binding after Aurora B inhibition may



1
2 **Figure 4. Aurora B kinase regulates NDC80-kMT binding in a graded fashion in vivo.**
3 (A) (top) Cell images showing mTurquoise2-NDC80 (blue) and beta-tubulin-TC-FIAsH (green). 5 μm
4 scale bar. (bottom) Time course of NDC80 FRET fraction in response to Aurora B inhibition by 3 μM
5 ZM447439 (n = 15 cells).
6 (B) (top) Cell images color-coded with Aurora B sensor non-FRET fraction. 5 μm scale bar. (bottom)
7 Time course of the non-FRET fraction of the cytoplasmic Aurora B FRET sensor in response to 3 μM
8 ZM447439 (n = 10 cells).
9 Black squares and error bars in (A) and (B) are the weighted mean and SEM of the data points (green
10 circles) in equally spaced time intervals of 1 minute. Red solid and dashed lines are the best-fit
11 exponential decay models and their 95% confidence intervals, respectively.
12 (C) NDC80 binding fraction (converted from NDC80 FRET fraction in (A)) plotted against the fraction of
13 phosphorylated Aurora B phosphorylation sites in NDC80 (converted from Aurora B FRET sensor non-
14 FRET fraction in (B)). Red solid and dashed lines are the best-fit NDC80-kMT binding model (derived in
15 Mathematical modeling in Methods) and its 95% confidence interval.

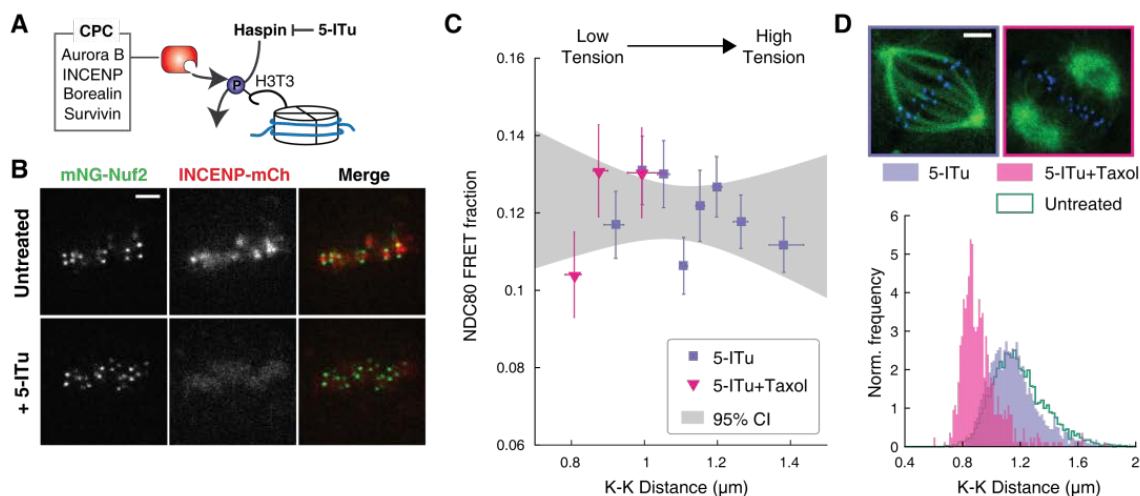
1 underlie the reduction in detachment of kMTs from kinetochores after Aurora B inhibition, observed in
2 photoactivation experiments (Cimini et al., 2006).

3

4 **Haspin-dependent centromere-localized Aurora B is responsible for the tension dependency of** 5 **NDC80-kMT binding**

6 Aurora B is localized to centromeres in prometaphase and metaphase, but its contribution to the tension-
7 dependent stabilization of kinetochore-microtubule attachments is controversial (Campbell and Desai,
8 2013, Salimian et al., 2011, Akiyoshi et al., 2010, Liu et al., 2009, Tanaka et al., 2002, Zaytsev et al.,
9 2016, Godek et al., 2015, Lampson and Cheeseman, 2011, Haase et al., 2017). To test the importance of
10 Aurora B localization at centromeres, we used the haspin kinase inhibitor, 5-iodotubercidin (5-ITu),
11 which has previously been shown to compromise the recruitment of Aurora B to inner-centromeres
12 (Wang et al., 2012) (Figure 5A). After 10 minutes of exposure of cells to 5-ITu, INCENP, a member of
13 the chromosome passenger complex (CPC), which also includes Aurora B (Carmena et al., 2012), was
14 drastically reduced at centromeres (Figure 5B). Treating cells with 5-ITu for over 15 minutes did not
15 significantly alter the average K-K distance ($1.16 \mu\text{m} \pm 0.18 \mu\text{m}$, 5-ITu vs. $1.19 \mu\text{m} \pm 0.19 \mu\text{m}$, untreated,
16 SD) or the overall average fraction of NDC80 bound to kMTs (FRET fraction, $11.79\% \pm 0.02\%$ 5-ITu vs.
17 $11.87\% \pm 0.02\%$, untreated, SEM), but eliminated the correlation between K-K distance and NDC80-
18 kMT binding (Figure 5C and D). In order to investigate a wider range of K-K distance, we treated cells
19 with both taxol and 5-ITu, and found no correlation over the full range of K-K distance (Figure 5C and D).
20 Thus, the tension-dependency of NDC80-kMT binding in human tissue culture cells depends on Aurora B
21 recruitment to centromeres by haspin kinase, arguing in favor of models in which phosphorylation by
22 Aurora B plays a central role in chromosome autonomous error correction.

23 We were surprised that the average NDC80-kMT binding does not significantly change after
24 mislocalizing Aurora B with 5-ITu (compare Figure 3D and 5C, and see Figure S7A). This suggests that
25 Aurora B can still act on NDC80 even after the concentration of Aurora B at centromeres is greatly



1
2 **Figure 5. Haspin-dependent centromere-localized Aurora B is responsible for the tension**
3 **dependency of NDC80-kMT binding**
4 (A) Haspin kinase phosphorylates histone H3 at Thr3 (H3T3), which recruits the chromosome passenger
5 complex (CPC, red) to centromeres. 5-Iodotubercidin (5-ITu) inhibits haspin kinase, thereby displacing
6 Aurora B from centromeres.
7 (B) Spinning-disk confocal microscopy images of cells expressing mNeonGreen-Nuf2 (green) and
8 INCENP-mCherry (red) before (top) and after (bottom) haspin inhibition by 10 μ M 5-ITu treatment. 3
9 μ m scale bar.
10 (C) NDC80 FRET fraction vs. K-K distance for cells treated with 10 μ M 5-ITu (purple square, n = 12
11 cells, 1016 kinetochores/data point) and with both 10 μ M 5-ITu and 10 μ M taxol (pink triangle, n = 3
12 cells, 359 kinetochores/data point). Data points are the mean, y-error bars the SEM, and the x-error bars
13 the interquartile ranges within groups of kinetochores with similar K-K distances. Gray area is the 95%
14 confidence interval for the linear fit to the combined data.
15 (D) Histograms of K-K distances for the 5-ITu-treated (pink), 5-ITu+taxol-treated (purple), and untreated
16 cells (green line). 3 μ m scale bar in the cell images of mTurquoise2-NDC80 (blue) and beta-tubulin-TC-
17 FAsH (green).

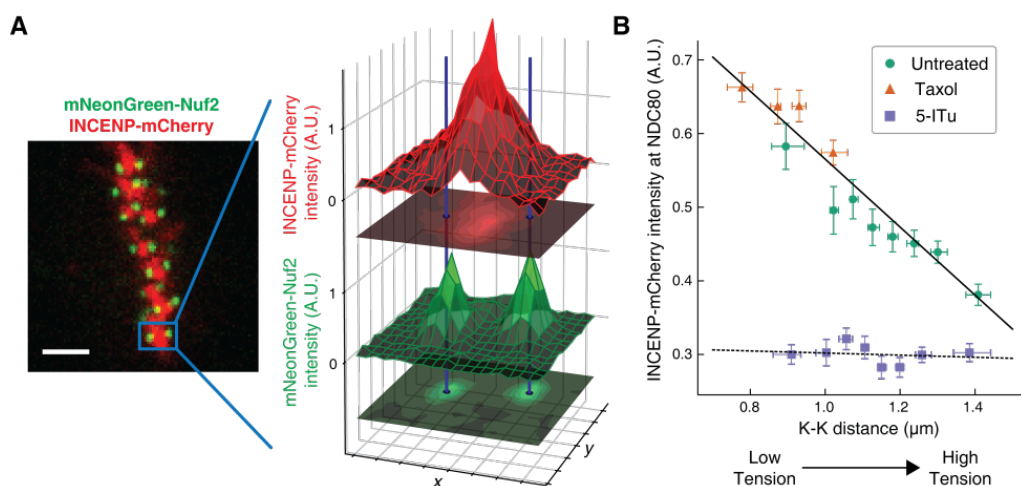
1 reduced. Consistent with this hypothesis, the Aurora B activity at kinetochores assessed by Nuf2-targeted
2 Aurora B FRET sensor was not changed by 5-ITu treatment (Figure S7B). Furthermore, when cells
3 treated with 5-ITu were exposed to the Aurora B inhibitor ZM447439, NDC80-kMT binding increased
4 (to NDC80 FRET fraction of 0.17 ± 0.01 , SEM) and Aurora B activity at kinetochores decreased (to
5 Aurora B FRET sensor non-FRET fraction of 0.55 ± 0.01 , SEM), indistinguishable from the levels in
6 cells not subject to 5-ITu exposed to ZM447439 (Figure S7). Thus, tension dependency of NDC80-kMT
7 binding is conferred by Aurora B recruited to centromeres through a haspin-dependent pathway, while the
8 average level of NDC80-kMT binding is also set by Aurora B, but in a manner that is not dependent on
9 haspin.

10

11 **The concentration of Aurora B at the location of NDC80 is dependent on centromere tension**

12 The extent to which Aurora B phosphorylates NDC80 depends on the activity of Aurora B and the
13 concentration of Aurora B at NDC80. To further investigate how the haspin-dependent pool of Aurora B
14 confers tension dependency to NDC80-kMT binding, we next examined how Aurora B localization
15 depends on K-K distance. We used spinning-disk confocal microscopy to image mNeonGreen-Nuf2, to
16 locate NDC80, and INCENP-mCherry, to measure the distribution of Aurora B. We localized NDC80 to
17 sub-pixel accuracy and identified sister kinetochore pairs (see Figure 6A and Methods). For each pair of
18 kinetochores, we measured the intensity of INCENP-mCherry at the location of NDC80, normalized on a
19 cell-by-cell basis. Plotting the intensity of INCENP-mCherry at NDC80 as a function of K-K distance
20 revealed a highly statistically significant anti-correlation ($p < 10^{-4}$, Figure 6B). To explore a larger range
21 of K-K distances, we treated cells with 10 μ M taxol. Combining the data of untreated and taxol-treated
22 cells, we found that the intensity of INCENP-mCherry at NDC80 linearly decreases with K-K distance
23 over the full range of K-K distance ($p < 10^{-6}$). This observation suggests that the tension dependency of
24 NDC80 binding may result from the decrease of Aurora B at NDC80 with increasing K-K distance.

25 We next investigated how the concentration of Aurora B at the location of NDC80 is influenced



1
2 **Figure 6. The concentration of Aurora B at the location of NDC80 decreases with centromere**
3 **tension.**
4 (A) Spinning-disk confocal microscopy image of mNeonGreen-Nuf2 (green) and INCENP-mCherry (red).
5 3 μm scale bar. The location of NDC80 was determined to sub-pixel accuracy, using the mNeonGreen-
6 Nuf2 image. For each pair of sister kinetochores, the intensity of INCENP-mCherry at the location of
7 NDC80 was measured and normalized on a cell-by-cell basis.
8 (B) Normalized INCENP-mCherry intensity at the location of NDC80 were averaged within groups of
9 kinetochores with similar K-K distances, and plotted against the K-K distances for untreated (green
10 circles), taxol-treated (orange triangles), and 5-ITu-treated (purple squares) cells. Data points are the
11 mean, y-error bars the SEM, and the x-error bars the interquartile ranges. Black solid and dotted lines are
12 the linear fits to DMSO+taxol combined data and 5-ITu data, respectively.
13 906 kinetochore pairs in 9 cells, 599 pairs in 8 cells, and 680 pairs in 6 cells were analyzed for DMSO
14 control, taxol treatment, and 5-ITu treatment data, respectively.

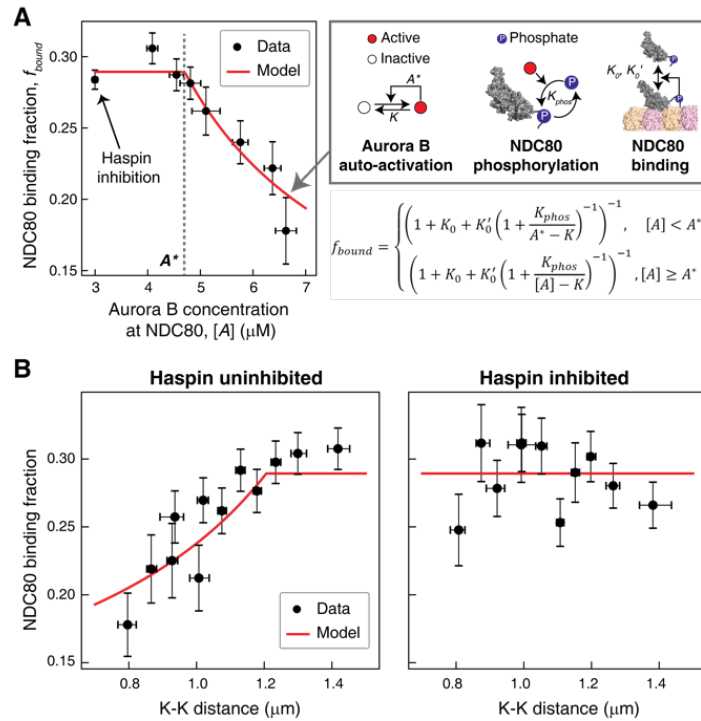
1 by haspin inhibition. In the presence of 10 μM 5-ITu, the concentration of Aurora B at NDC80 was
2 greatly reduced and independent of K-K distance (Figure 6B). The lack of correlation between Aurora B
3 concentration at NDC80 and K-K distance may explain the lack of tension dependency between NDC80-
4 kMT binding and K-K distance upon haspin inhibition. We speculate that the finite concentration of
5 Aurora B at NDC80 after haspin inhibition is the pool of Aurora B that maintains the average level of
6 NDC80-kMT binding as described above.

7

8 **A biophysical model of tension dependent NDC80-kMT binding**

9 Taking together, our data suggest that the concentration of Aurora B at NDC80 determines the extent of
10 NDC80 phosphorylation, which in turn determines the level of NDC80-kMT binding. To further explore
11 this possibility, we sought to determine the relationship between Aurora B concentration at NDC80 and
12 NDC80-kMT binding. We plotted the NDC80-kMT binding (converted from the NDC80 FRET fraction
13 in Figure 3D and 5C) vs. the Aurora B concentration (converted from the normalized INCENP-mCherry
14 intensity in Figure 6D) for each K-K distance, both with and without haspin inhibition (Figure 7A, see
15 Methods). This revealed a highly nonlinear relationship: when the Aurora B concentration is lower than
16 $\sim 5 \mu\text{M}$, the NDC80 binding fraction is independent of the Aurora B concentration, while for higher
17 concentrations, the NDC80 binding fraction decreases with the Aurora B concentration (Figure 7A).

18 We constructed a mathematical model to determine if this nonlinear relationship can be explained
19 by the known biochemistry of Aurora B and NDC80 (Figure 7A). In this model, we assume that there are
20 two independent pools of Aurora B, haspin-dependent and haspin-independent, both of which engage in
21 intermolecular autoactivation by phosphorylation in *trans* (Zaytsev et al., 2016, Xu et al., 2010, Sessa et
22 al., 2005, Bishop and Schumacher, 2002), and are inactivated by phosphatases (Zaytsev et al., 2016, Sessa
23 et al., 2005, Kelly et al., 2007, Rosasco-Nitcher et al., 2008). The activated Aurora B phosphorylates
24 NDC80, which changes the binding affinity of NDC80 for kMTs (Cheeseman et al., 2006, Zaytsev et al.,
25 2014, Zaytsev et al., 2015). This model can be solved analytically, and is sufficient to account for the



1
2 **Figure 7. A biophysical model of tension dependent NDC80-kMT binding**
3 (A) Plot of NDC80 binding fraction, f_{bound} (converted from NDC80 FRET fraction in Figure 3D and 5C)
4 vs. Aurora B concentration at NDC80, $[A]$ (converted from INCENP-mCherry intensity in Figure 6B, see
5 Methods). Data points (black circles) are the mean and SEM. We constructed a mathematical model that
6 predicts NDC80 binding fraction from Aurora B concentration at NDC80 through three steps:
7 intermolecular Aurora B auto-activation, NDC80 phosphorylation, and NDC80-kMT binding. Red line
8 shows the mathematical model fit to the data.
9 (B) NDC80 binding fraction vs. K-K distance before (left) and after (right) haspin inhibition by 5-ITu.
10 The data points (black circles) are adapted from Figure 3D and 5C. Red lines are the predictions from the
11 mathematical model.

1 relationship between NDC80 phosphorylation and NDC80-kMT binding (Figure 4C), and the relationship
2 between Aurora B concentration at NDC80 and NDC80-kMT binding (Figure 7A). In this model, the
3 nonlinear relationship between Aurora B concentration at NDC80 and NDC80-kMT binding ultimately
4 results from the activation dynamics of Aurora B: at low concentrations, dephosphorylation by
5 phosphatases overwhelm the *in trans* autoactivation, but above a threshold Aurora B concentration, A^* ,
6 these two processes balance, leading to steady state level of activated Aurora B that further increases with
7 increasing Aurora B concentration.

8 We next investigated if the same model can recapitulate the tension dependency of NDC80-kMT
9 binding. We combined all data from Figure 3D and converted the NDC80 FRET fraction to NDC80
10 binding fraction. Inputting the measured linear relationship between Aurora B concentration at NDC80
11 and K-K distance (Figure 6B) into the model reproduced the observed tension-dependent behavior of
12 NDC80-kMT binding (Figure 7B, left). Performing a similar procedure with the data from haspin
13 inhibited cells (Figure 5C and 6B) revealed that the model successfully predicts both the level of NDC80-
14 kMT binding upon haspin inhibition and its independence on K-K distance (Figure 7B, right). Thus, this
15 model provides a self-consistent, quantitative explanation of how the tension dependency of NDC80-kMT
16 binding results from the biochemistry of Aurora B and NDC80.

17

18

19 **DISCUSSION**

20 In this study, we developed a method to quantitatively measure the binding of the NDC80 complex to
21 microtubules at individual kinetochores in human tissue culture cells. Our method uses TCSPC FLIM-
22 FRET which, in contrast to intensity-based FRET, allows quantitative measurements of the fraction of
23 molecules engaging in FRET, even with spatially varying concentrations of donors and acceptors. We
24 calibrated our measurements using control experiments and Monte Carlo simulations, allowing us to
25 convert the fraction of donor-labeled Nuf2 engaged in FRET to the fraction of NDC80 complexes bound

1 to kMTs. This technique can be extended to the quantitative assessment of other protein-protein
2 interactions in living cells.

3 Using this technique, we demonstrated that NDC80-kMT binding is regulated during
4 prometaphase in a chromosome-autonomous manner. We observed that NDC80-kMT binding is strongly
5 correlated to centromere tension, to an extent which is sufficient to account for the changes in NDC80-
6 kMT binding over the course of prometaphase and metaphase. We characterized how Aurora B modulates
7 NDC80-kMT binding in cells, and found that the concentration of Aurora B at the locations of NDC80
8 decreases with increasing centromere tension. Mislocalizing Aurora B by inhibiting haspin kinase
9 eliminated the tension dependency of NDC80-kMT binding, but did not change its average level. The
10 observation that inhibiting haspin removes the correlations between NDC80-kMT binding and tension
11 and between Aurora B localization and tension, but does not affect the distribution of K-K distances,
12 argues that these correlations are caused by the influence of tension on NDC80-kMT binding and Aurora
13 B localization. A simple mathematical model of Aurora B autoactivation, and NDC80 phosphorylation
14 and binding can quantitatively explain these results. Taking together, this leads to a biophysical model of
15 the tension dependency of NDC80-kMT interactions, which arises from the nonlinearity of Aurora B
16 autoactivation and the change in Aurora B concentration at NDC80 with centromere tension.

17 Error correction is believed to result from the regulation of the detachment of kMTs from
18 kinetochores (Godek et al., 2015). As NDC80 is the primary coupler of kinetochores to microtubules
19 (Cheeseman et al., 2006, DeLuca et al., 2006), it is reasonable to hypothesize that the rate of kMT
20 detachment from kinetochores might largely be governed by NDC80-kMT binding. Consistent with this,
21 previous work showed that mutating NDC80 changes the number of kMTs in a manner that argues that
22 increasing NDC80-kMT binding increases the stability of kMTs (Guimaraes et al., 2008, Zaytsev et al.,
23 2014). Our work further supports the connection between NDC80-kMT binding and kMT stability by
24 comparing our results with previous measurements of the rate of kMT detachment from kinetochores:
25 NDC80-kMT binding increases during mitotic progression (Figure 2), while kMT stability increases

1 (Zhai et al., 1995, Kabeche and Compton, 2013); NDC80-kMT binding increases in response to Aurora B
2 inhibition (Figure 4), which causes an increase in kMT stability (Cimini et al., 2006); NDC80
3 preferentially binds to polymerizing kMTs over depolymerizing kMTs (Figure 3C), while reconstituted
4 kinetochores bind more strongly to polymerizing microtubules than depolymerizing microtubules
5 (Akiyoshi et al., 2010); NDC80-kMT binding increases with increasing tension (Figure 3D), and the
6 stability of kMTs increase with increasing tension (Nicklas and Koch, 1969, Akiyoshi et al., 2010). These
7 comparisons argue that the NDC80-kMT binding is a major determinant of the kMT detachment rate.
8 Hence, we propose that tension dependency of kMT detachment from kinetochores, which is believed to
9 underlie error correction, results from the tension dependency of NDC80-kMT binding. If correct, this
10 implies that error correction ultimately results from the nonlinear autoactivation of Aurora B and the
11 consequent phosphoregulation of NDC80-kMT binding. Further testing this proposal will require
12 additional quantitative measurements of kMT detachment, errors, and error correction, in combination
13 with measurement of NDC80-kMT binding using the FLIM-FRET method presented here.

1 **MATERIALS AND METHODS**

2

3 **Cell culture**

4 U2OS cell lines were maintained in Dulbecco's modified Eagle's medium (DMEM, Thermo Fisher)
5 supplemented with 10% Fetal Bovine Serum (FBS, Thermo Fisher), and 50 IU ml⁻¹ penicillin and 50 µg
6 ml⁻¹ streptomycin (Thermo Fisher) at 37°C in a humidified atmosphere with 5% CO₂. Cells were
7 validated as mycoplasma free by PCR-based mycoplasma detection kit (Sigma Aldrich).

8

9 **Live-cell imaging**

10 All live-cell FLIM and spinning-disk confocal microscopy imaging were performed as follows. Cells
11 were grown on a 25-mm diameter, #1.5-thickness, round coverglass coated with poly-D-lysine (GG-25-
12 1.5-pdl, neuVibro) to 80~90% confluency. The cells were incubated in imaging media, which is
13 FluoroBrite™ DMEM (Thermo Fisher) supplemented with 4 mM L-glutamine (Thermo Fisher) and 10
14 mM HEPES, for 15~30 minutes before imaging. The coverglass was mounted on a custom-built
15 temperature controlled microscope chamber at 37°C, while covered with 1 ml of imaging media and 2 ml
16 of white mineral oil (VWR). An objective heater (Biotech) was used to maintain the objective at 37°C.
17 We confirmed that the cells can normally divide longer than 6 hours in this condition. Only cells
18 displaying proper chromosome alignment, normal spindle morphology, and high signal-to-noise ratio
19 were selected for imaging and analysis.

20

21 **NDC80-kMT FLIM-FRET measurement**

22 mTurquoise2-NDC80/β-tubulin-TC-FIAsH stable U2OS cell line

23 A tetracysteine (TC) tag, CCPGCC, was genetically attached to the C-terminal end of tubulin beta class I
24 (TUBB), an isotype of β-tubulin that is predominantly expressed in U2OS (assessed by qPCR, data not
25 shown) and most other cancer cells (Leandro-Garcia et al., 2010). The attachment of the TC tag was
26 achieved by CRISPR-induced homologous recombination to ensure the consistent expression of labeled

1 β -tubulin. ssDNA (IDT) with TC tag (5'-TGCTGTCCCGGCTGTTGC-3') and ~80 bp-long homology
2 arms was used as a donor DNA. pSpCas9(BB)-2A-GFP (Addgene plasmid # 48138) (Ran et al., 2013)
3 was utilized as a backbone for the plasmid carrying a sgRNA (5'-GAGGCCGAAGAGGAGGCCUA-3')
4 and Cas9. The plasmid and the donor ssDNA were simultaneously delivered into U2OS cells by
5 electroporation (Nucleofector™ 2b and Amaxa Cell Line Nucleofector Kit V, Lonza). The insertion of the
6 TC tag was verified through a PCR-based genotyping with primers 5'-
7 GCATGGACGAGATGGAGTTCAC-3' and 5'-CCAGCCGTGTTCCCTAAATAAG-3', qPCR, and a
8 fluorescence imaging after FIAsh-EDT₂ staining.

9 The U2OS cells expressing TC-tagged β -tubulin were further engineered to stably express Nuf2
10 N-terminally labeled with mTurquoise2 (Goedhart et al., 2012) by retroviral transfection, three times with
11 different antibiotic selections, 1 $\mu\text{g ml}^{-1}$ puromycin, 2 $\mu\text{g ml}^{-1}$ blasticidin, and 200 $\mu\text{g ml}^{-1}$ hygromycin (all
12 from Thermo Fisher). The retroviral vectors and their information are available on Addgene (plasmid #:
13 80760, 80761, 80762). Monoclonal cell line was obtained by single cell sorting.

14

15 FIAsh-EDT₂ staining

16 The protocol for the association of FIAsh-EDT₂ with β -tubulin-TC in cell was adapted from the previous
17 study (Hoffmann et al., 2010) so as to maximize the labeling fraction while maintaining cell viability. The
18 engineered U2OS cells expressing β -tubulin-TC were grown to 80~90% confluency in a 30-mm cell
19 culture dish, and then were gently washed with Opti-MEM (Thermo Fisher) twice, and then stained in 2
20 ml Opti-MEM with 1 μM FIAsh-EDT₂ (Thermo Fisher) for 2 hours. To reduce the non-specific binding
21 of FIAsh, the stained cells were subsequently incubated in Opti-MEM containing 250 μM 1,2-
22 Ethanedithiol (EDT, Alfa Aesar) for 10 minutes, followed by a gentle wash with Opti-MEM. The cells
23 were incubated in DMEM with 10% FBS for 6~10 hours before imaging, because they were found to be
24 interphase-arrested for the first ~5 hours after the incubation with 250 μM EDT. Every buffers and media

1 above were pre-warmed at 37°C before use. All incubation steps were performed at 37°C in a humidified
2 atmosphere with 5% CO₂.

3

4 FLIM measurement

5 Schematic instrumental setup of FLIM is shown in Figure S1A, and more details can be found in previous
6 work (Yoo and Needleman, 2016). FLIM measurements were performed on a Nikon Eclipse Ti
7 microscope using two-photon excitation from a Ti:Sapphire pulsed laser (Mai-Tai, Spectral-Physics) with
8 an 80-MHz repetition rate and ~70-fs pulse width, a galvanometer scanner (DCS-120, Becker & Hickl),
9 TCSPC module (SPC-150, Becker & Hickl) and two hybrid detectors (HPM-100-40, Becker & Hickl).
10 Objective piezo stage (P-725, Physik Instrumente) and motorized stage (ProScan II, Prior Scientific) were
11 used to perform multi-dimensional acquisition, and a motor-driven shutter (Sutter Instrument) was used to
12 block the excitation laser between acquisitions. The wavelength of the excitation laser was set to 865 nm.
13 470/24 and 525/30 bandpass emission filters (Chroma) were mounted on each detector, and a dichroic
14 beam splitter (FF506-Di03, Semrock) was used for the simultaneous detection of mTurquoise2 and
15 FAsH fluorescence. The excitation laser was expanded to overfill the back-aperture of a water-immersion
16 objective (CFI Apo 40× WI, NA 1.25, Nikon). The power of the excitation laser was adjusted to 1.1~1.5
17 mW at the objective. All the electronics were controlled by SPCM software (Becker & Hickl) and
18 μManager (Edelstein et al., 2014). Scanning area was set to either 13.75 μm × 13.75 μm or 27.5 μm ×
19 27.5 μm, and the pixel size was set to 107 nm. Each image was acquired for 3~5 seconds of integration
20 time. Acquisition interval was set to 13 seconds for Figure 2 and 4, and 60~90 seconds for Figure 3, 5,
21 and S6. Three or four z-sections, separated by 1 μm, were acquired for each time point. No photo-
22 bleaching or photo-damage was observed in this imaging condition.

23

24 Kinetochore tracking and pairing

1 For the kinetochore FLIM-FRET measurements shown in Figure 2 to 5, custom-built MATLAB graphical
2 user interphase (GUI) was used to import Becker and Hickl FLIM data, track kinetochores, identify
3 kinetochore pairs, extract the FLIM curve from each kinetochore, and estimate the FLIM parameters
4 using a nonlinear least-squared fitting or Bayesian FLIM analysis, as described below and in previous
5 work (Yoo and Needleman, 2016). The GUI (available at [https://github.com/taebong/FLIM-Interactive-](https://github.com/taebong/FLIM-Interactive-Data-Analysis)
6 [Data-Analysis](https://github.com/taebong/FLIM-Interactive-Data-Analysis)) also allows the users to scrutinize and manually correct the kinetochore trajectories and
7 pairing. The kinetochore tracking algorithm was adapted from a particle tracking algorithm (Pelletier et
8 al., 2009), and the pair identification was performed by selecting pairs of kinetochores with distances and
9 velocity correlations in predefined ranges. Correction for spindle movement is done by measuring
10 correlation between two consecutive spindle images. The velocity $v(t)$ of kinetochore (in Figure 3) was
11 estimated from the position $x(t)$ using the five-point method:

$$v(t) \approx \frac{-x(t + 2\Delta t) + 8x(t + \Delta t) - 8x(t - \Delta t) + x(t - 2\Delta t)}{12\Delta t}$$

12 The metaphase plate (in Figure 2) was determined by finding an equidistant plane between the two
13 spindle poles (that were manually located).

14

15 Bayesian FLIM analysis

16 Fluorescence decay curves from individual kinetochores at each time point contain only a few hundreds
17 of photons. In this low photon count regime, FLIM analysis with conventional least-squared nonlinear
18 regressions results in significantly biased estimate for the parameters (Kaye et al., 2017, Rowley et al.,
19 2016). Therefore, we used a Bayesian approach, which has been described and tested previously (Yoo and
20 Needleman, 2016, Kaye et al., 2017), and is briefly explained below.

21 Let θ be the set of parameters of the FLIM-FRET model, and $y = \{y_i\}$ be the observed FLIM
22 data, where y_i is the number of photons detected in the i -th time bin of the FLIM curve. Then the
23 posterior distribution of θ (assuming a uniform prior distribution) is

$$p(\theta|y) \propto \prod_{i=1}^N P(t_{ar} \in [(i-1)\Delta t, i\Delta t]|\theta)^{y_i}$$

1 where t_{ar} is the photon arrival time, and N is the number of time bins. Since the size of the time bin (Δt ,
 2 ~ 50 ps) is much smaller than the time scale of fluorescence decay (\sim ns), the probability that the arrival
 3 time t_{ar} falls in the i -th time bin can be approximated by a Riemann sum:

$$P(t_{ar} \in [(i-1)\Delta t, i\Delta t]|\theta) \cong \sum_{k=(i-1)K+1}^{iK} h_{\theta}(k\widetilde{\Delta t})\widetilde{\Delta t}$$

4 where h_{θ} is the discretized FLIM model, $\widetilde{\Delta t}$ is the size of time bin with which instrument response
 5 function (IRF) is measured, and the ratio $K = \frac{\Delta t}{\widetilde{\Delta t}}$ is the ADC ratio, which is set to 16 for our data.
 6 $h_{\theta}(k\widetilde{\Delta t})$ can be written as the convolution between the IRF and an exponential decay model, g_{θ} :

$$\begin{aligned} h_{\theta}(k\widetilde{\Delta t}) &= (IRF * (Ag_{\theta} + (1-A)))(k\widetilde{\Delta t}) \\ &\cong \sum_l mIRF[l - b_{shift}](Ag_{\theta}((k-l)\widetilde{\Delta t}) + (1-A)) \end{aligned}$$

7 where $mIRF$ is the IRF measured with the finest time bins of size $\widetilde{\Delta t}$, and b_{shift} is an integer parameter
 8 that determines the approximate shift of measured IRF relative to the theoretical IRF. $(1-A)$ indicates
 9 the relative contribution of noise that is uniformly distributed over time. The exponential decay model
 10 $g_{\theta}(t_d)$ is set to $\exp\left(-\frac{t_d}{\tau}\right)$ for the single-exponential decay model or $(1-f_{FRET})e^{-\frac{t_d}{\tau_D}} + f_{FRET}e^{-\frac{t_d}{\tau_{FRET}}}$
 11 for the two-exponential decay model, where $0 \leq f_{FRET} \leq 1$ is the FRET fraction. The posterior
 12 distribution was computed by Gibbs sampling if the number of free parameters is greater than 3, or by
 13 grid sampling otherwise (for example, when both long and short lifetimes are fixed).

14

15 NDC80 FRET fraction measurement procedures

16 The instrument response function (IRF) was acquired by measuring second-harmonic generation from a
 17 urea crystal. Negative control FLIM measurements on the engineered cells (mTurquoise2-NDC80/ β -

1 tubulin-TC) not incubated with FIAsh were performed for every experiment and the fluorescence decay
2 curves extracted from kinetochores were analyzed with a single-exponential FLIM-FRET model to
3 determine the long non-FRET lifetime, which is usually 3.7 to 3.8 ns. The short FRET lifetime was
4 estimated by performing a two-exponential Bayesian FLIM-FRET analysis on the aggregated FLIM data
5 of kinetochores in each cell stained with FIAsh while fixing the non-FRET lifetime to the value pre-
6 determined from the negative control. Then we performed a two-exponential Bayesian FLIM-FRET
7 analysis, with both FRET and non-FRET lifetimes fixed to the predetermined values, on FLIM data from
8 each kinetochore. Kinetochores were grouped by time (Figure 2A, and 4), positions (Figure 2B-D),
9 velocities (Figure 3C), and K-K distances (Figure 3D and 5C). The posterior distributions in a group of
10 kinetochores were multiplied and then marginalized to obtain the mean and SEM of the FRET fraction.
11 We previously confirmed that this way of combining posterior distribution gives an unbiased estimate of
12 the mean FRET fraction (Kaye et al., 2017). NDC80 binding fraction was calculated by dividing NDC80
13 FRET fraction by the conversion factor 0.42, which had been determined by the calibration shown in
14 Figure S4C.

15

16 **Aurora B kinase activity measurement**

17 An Aurora B FRET sensor was constructed by replacing CyPet in a previous construct (Addgene plasmid
18 # 45215) (Fuller et al., 2008) with mTurquoise2. The FRET sensor contains a kinesin-13 family Aurora B
19 substrate whose phosphorylation results in its binding to the forkhead-associated domain in the sensor,
20 which constrains the sensor to be in an open conformation and obstructs intramolecular FRET between
21 mTurquoise2 and YPet (Figure S6B). Hence, the non-FRET fraction of the Aurora B FRET sensor is
22 proportional to the Aurora B activity. The cytoplasmic Aurora B FRET sensor was stably expressed in
23 U2OS cells by retroviral transfection (plasmid available on Addgene, plasmid # 83286). The nuf2-
24 targeted Aurora B FRET sensor was transiently transfected by electroporation (Nucleofector 2b, Lonza;
25 Ingenio Electroporation Kit, Mirus) a day before imaging. The non-FRET fraction of the Aurora B FRET

1 sensor was measured by FLIM-FRET in the same way as NDC80 FRET measurements described above.
 2 The exponential decay models $y_{\text{binding}}(t) = A_1 \left(1 - \exp\left(-\frac{I_{t \geq 0} t}{\tau_1}\right)\right) + c_1$ and $y_{\text{Aurora}}(t) =$
 3 $A_2 \exp\left(-\frac{I_{t \geq 0} t}{\tau_2}\right) + c_2$ were fitted to the time courses of NDC80 FRET fraction and FRET sensor non-
 4 FRET fraction after ZM447439, respectively (Figure 4A and B), where $I_{t \geq 0}$ is equal to 0 if t is less than
 5 zero, and 1 otherwise. The estimated parameter values are given in the table below:

	mean	95% CI
A_1	0.088	(0.069,0.106)
τ_1 (min)	3.26	(1.31,5.21)
c_1	0.089	(0.080,0.099)
A_2	0.17	(0.16,0.18)
τ_2 (min)	1.95	(1.46,2.45)
c_2	0.37	(0.36,0.38)

6 The fraction of Aurora B phosphorylation sites in NDC80, f_{phos} (x-axis of Figure 4C), was converted
 7 from the non-FRET fraction of Aurora B FRET sensor, f_{sensor} (y-axis of Figure 4B), as follows. First, we
 8 assumed that f_{sensor} increases linearly with f_{phos} . Previous work suggested that Ndc80 has about one
 9 phosphor-residue out of nine phosphorylation sites in late prometaphase (Zaytsev et al., 2014), based on
 10 which we assumed that $f_{\text{phos}}^{\text{WT}} = 1/9$ before Aurora B inhibition, and $f_{\text{phos}}^{\text{ZM}} = 0$ after the full Aurora B
 11 inhibition. Since f_{sensor} were measured to be $f_{\text{sensor}}^{\text{WT}} = 0.540 \pm 0.007$ (SEM) before Aurora B inhibition
 12 and $f_{\text{sensor}}^{\text{ZM}} = 0.368 \pm 0.012$ (SEM) after the full Aurora B inhibition (Figure 4B), we converted f_{sensor}
 13 to f_{phos} by:

$$f_{\text{phos}} = \frac{f_{\text{sensor}} - f_{\text{sensor}}^{\text{ZM}}}{f_{\text{sensor}}^{\text{WT}} - f_{\text{sensor}}^{\text{ZM}}} (f_{\text{phos}}^{\text{WT}} - f_{\text{phos}}^{\text{ZM}}) + f_{\text{phos}}^{\text{ZM}} = 0.646(f_{\text{sensor}} - 0.368)$$

14 The f_{bound} vs f_{phos} data in Figure 4C was fit using a NDC80 binding model:

$$f_{\text{bound}} = (1 + K_0 + K'_0 f_{\text{phos}})^{-1}$$

15 which is derived in Mathematical modeling section below.

16

17 **Aurora B concentration at NDC80 measurement**

18 mNeonGreen-Nuf2/INCENP-mCherry U2OS cell

1 mNeonGreen fluorescent protein (Shaner et al., 2013) was genetically attached to the N-terminal end of
2 Nuf2 by CRISPR-induced homologous recombination with an sgRNA (5'-
3 GAAAGACAAAGTTTCCATCTTGG-3') and mNeonGreen sequence (Allele Biotechnology) flanked by
4 2kb homology arms as a donor template. Monoclonal cell line was obtained by fluorescence-activated cell
5 sorting and screened by fluorescent microscopy imaging. The mNeonGreen-Nuf2 U2OS cell line was
6 transiently transfected with INCENP-mCherry (gift from Michael Lampson) by electroporation
7 (Nucleofector 2b and Amaxa Cell Line Nucleofector Kit V, Lonza) a day before imaging, using the
8 manufacturer's protocol.

9 10 Spinning-disk confocal microscopy imaging

11 Cells were imaged using a spinning-disk confocal microscope (Nikon Ti2000, Yokugawa CSU-X1) with
12 1.5x magnification lens and 1.2x tube lens, an EM-CCD camera (Hamamatsu), a 60x water-immersion
13 objective (Nikon), an objective piezo stage (P-725, Physik Instrumente), and motorized x-y stage
14 (ProScan II, Prior Scientific) controlled by μ Manager (Edelstein et al., 2014). A 488-nm laser and 514/30
15 filter were used to image mNeonGreen-Nuf2, and a 560-nm laser and 593/40 filter were used to image
16 INCENP-mCherry. 11-15 z-slices, separated by 2 μ m, were taken for each time point. Three time points,
17 separated by a minute, were acquired before and after DMSO (for untreated data), 10 μ M taxol, or 10 μ M
18 5-ITu treatment.

19 20 Aurora B concentration at NDC80 measurement

21 Image analysis was performed by a Python software (available at
22 <https://github.com/taebong/AuroraConcentrationAnalysis>). Kinetochores identification was achieved by
23 applying *trackpy* package (github.com/soft-matter/trackpy) to mNeonGreen-Nuf2 fluorescence images.
24 The sub-pixel location of NDC80 was calculated by centroid estimation. Sister kinetochore pairs were
25 determined based on the relative positions of kinetochores and the INCENP-mCherry intensity between

1 kinetochores. For each identified kinetochore pair, INCENP-mCherry intensities at the NDC80 centroid
2 locations, I_{NDC80} , and INCENP-mCherry intensity at the midpoint between two sister kinetochores, I_{mid} ,
3 were measured by two-dimensional cubic interpolation with *scipy.interpolate.griddata* function. For each
4 cell, we used $\overline{I_{mid}}$, which is I_{mid} averaged over kinetochores in the images before chemical treatments,
5 and cytoplasmic background level, I_{bg} , to obtain normalized the INCENP-mCherry intensities at NDC80,
6 I_{NDC80}^{norm} , by:

$$I_{NDC80}^{norm} = \frac{I_{NDC80} - \overline{I_{mid}}}{\overline{I_{mid}} - I_{bg}}$$

7 Kinetochores with similar K-K distances were grouped in the same way as in Figure 3D and 5C, and then
8 the normalized INCENP-mCherry intensities at NDC80, I_{NDC80}^{norm} , were averaged within each group. The
9 normalized INCENP-mCherry intensity was converted to Aurora B concentration in Figure 7A by
10 assuming that $\overline{I_{mid}}$ corresponds to the peak Aurora B concentration, which had previously estimated to be
11 10 μM (Zaytsev et al., 2016).

12

13 **Drug treatments**

14 Cells were incubated with 5 μM Nocodazole (Sigma Aldrich) for >10 minutes for microtubule
15 depolymerization. Aurora B inhibition was performed by adding 3 μM of ZM447439 (Enzo Life Sciences)
16 during imaging. Taxol (Enzo Life Sciences) treatment was performed at 10 μM final concentration for
17 >10 minutes. For the haspin kinase inhibition, cells were treated with 10 μM 5-iodotubercidin (5-ITu,
18 Enzo Life Sciences) for >10 minutes. The double treatment of 5-ITu and taxol was performed
19 sequentially by treating cells with 10 μM taxol and then adding 10 μM 5-ITu.

20

21 **Mathematical modeling**

22 Here we describe the mathematical model presented in Figure 7 in detail. The model predicts NDC80
23 binding fraction from Aurora B concentration at NDC80 in three steps: (1) Aurora B activation dynamics,

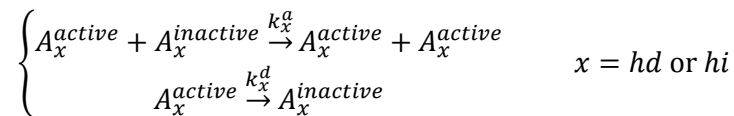
1 consisting of autoactivation in *trans* and deactivation, which determines the concentration of *active*
 2 Aurora B from the concentration of Aurora B; (2) NDC80 phosphorylation, which is dependent on the
 3 active Aurora B concentration; and (3) NDC80-kMT binding, which is governed by the phosphorylation
 4 level of NDC80.

5

6 (1) Aurora B activation

7 In this section, we present a quantitative model for the relationship between the Aurora B concentration
 8 (which we measured in Figure 6) and the *active* Aurora B concentration (which determines the steady-
 9 state level of NDC80 phosphorylation). It has been previously argued that Aurora B activation is
 10 predominately due to active Aurora B phosphorylating inactive Aurora B in *trans* (Zaytsev et al., 2016,
 11 Xu et al., 2010, Sessa et al., 2005, Bishop and Schumacher, 2002), which we incorporate into our model.
 12 We model Aurora B at the location of NDC80 as consisting of two separate pools: one that is dependent
 13 on haspin, and the other that is not. We assume that those two Aurora B pools do not interact with each
 14 other, and independently undergo auto-activation in *trans*. We further assume that the phosphatases
 15 activity proceeds at a constant rate for each pool.

16 We denote the haspin-dependent and haspin-independent pools of Aurora B by A_{hd} and A_{hi} ,
 17 respectively. Then the inter-molecular autoactivation by in *trans* phosphorylation and inactivation by
 18 dephosphorylation for each of the two Aurora B pools are described by:



19 where A_x^{active} and $A_x^{inactive}$ are the active and inactive Aurora B in pool x , respectively, and k_x^a and k_x^d
 20 are the rates of Aurora B activation and deactivation for the pool x , respectively. Thus, an ordinary
 21 differential equation (ODE) for active Aurora B concentration can be written as:

$$\frac{\partial [A_x^{active}]}{\partial t} = k_x^a [A_x^{active}] [A_x^{inactive}] - k_x^d [A_x^{active}]$$

$$\begin{aligned}
 &= k_x^a [A_x^{active}] ([A_x] - [A_x^{active}]) - k_x^d [A_x^{active}] \\
 &= k_x^a [A_x^{active}] \left([A_x] - \frac{k_x^d}{k_x^a} - [A_x^{active}] \right)
 \end{aligned}$$

- 1 where $[A_x] = [A_x^{active}] + [A_x^{inactive}]$ is the concentration of the pool x . The steady-state solution for this
 2 ODE is:

$$[A_x^{active}] = \begin{cases} 0, & [A] < K_x \\ [A_x] - K_x, & [A] \geq K_x \end{cases}$$

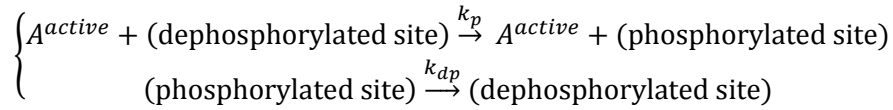
- 3 where $K_x \equiv k_x^d/k_x^a$ is the equilibrium constant for the Aurora B activation for pool x . We can infer that
 4 $[A_{hi}^{active}] = [A_{hi}] - K_{hi}$ is positive, because Aurora B still acts on NDC80 after the removal of the
 5 haspin-dependent pool (Figure 5 and S7). Therefore, the total concentration of active Aurora B at NDC80
 6 can be written as:

$$\begin{aligned}
 [A^{active}] &= [A_{hd}^{active}] + [A_{hi}^{active}] \\
 &= \begin{cases} [A_{hi}] - K_{hi}, & [A] < K_{hd} + [A_{hi}] \\ [A] - K_{hd} - K_{hi}, & [A] \geq K_{hd} + [A_{hi}] \end{cases} \\
 &= \begin{cases} A^* - K, & [A] < A^* \\ [A] - K, & [A] \geq A^* \end{cases} \quad (\text{Eq. 1})
 \end{aligned}$$

- 7 where $[A] = [A_{hd}] + [A_{hi}]$ is the total concentration of Aurora B at NDC80, $K = K_{hd} + K_{hi}$, and
 8 $A^* = K_{hd} + [A_{hi}]$ is a threshold Aurora B concentration, which is the minimum concentration of Aurora
 9 B required for the activity of Aurora B to increase with its concentration.

10
 11 (2) NDC80 phosphorylation

- 12 In this section, we present a mathematical model to relate the total concentration of active Aurora B at
 13 NDC80, $[A^{active}]$, to the phosphorylation level of NDC80. Active Aurora B may phosphorylate multiple
 14 Aurora B phosphorylation sites in each Ndc80 N-terminal tail (Guimaraes et al., 2008), which we
 15 describe with the equations:



1 The corresponding ODE for the number of phosphorylated sites is:

$$\begin{aligned} \frac{\partial N_p}{\partial t} &= k_p [A^{active}] N_{dp} - k_{dp} N_p \\ &= k_p [A^{active}] (N - N_p) - k_{dp} N_p \end{aligned}$$

2 where N_p , N_{dp} , and $N = N_p + N_{dp}$ is the number of phosphorylated sites, dephosphorylated sites, and the

3 total number of sites per kinetochore, respectively. The steady-state solution for the ODE gives:

$$f_{phos} = \frac{N_p}{N} = \left(1 + \frac{K_{phos}}{[A^{active}]} \right)^{-1} \quad (\text{Eq. 2})$$

4 where f_{phos} is the fraction of phosphorylated sites, and $K_{phos} \equiv \frac{k_{dp}}{k_p}$ is the equilibrium constant for

5 NDC80 phosphorylation. Plugging Eq. 1 into Eq. 2 yields:

$$f_{phos} = \begin{cases} \left(1 + \frac{K_{phos}}{A^* - K} \right)^{-1}, & [A] < A^* \\ \left(1 + \frac{K_{phos}}{[A] - K} \right)^{-1}, & [A] \geq A^* \end{cases} \quad (\text{Eq. 3})$$

6

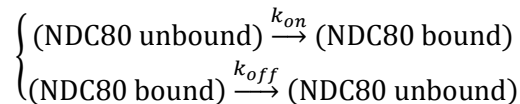
7 (3) NDC80 binding

8 In this section, we present a model to relate the fraction of phosphorylated sites in NDC80 per

9 kinetochore, f_{phos} , to the fraction of NDC80 bound to kMTs (which we measure using FLIM-FRET).

10 Assuming that the number of available binding sites for NDC80 is constant, we may describe the NDC80

11 binding and unbinding by the following equations:



12 The corresponding ODE for the number of NDC80 bound to kMTs is:

$$\frac{\partial n_{on}}{\partial t} = k_{on} n_{off} - k_{off} n_{on}$$

$$= k_{on}(n - n_{on}) - k_{off}n_{on}$$

1 where n_{on} and n_{off} are the number of NDC80 bound and unbound to kMTs, respectively, and $n =$
 2 $n_{on} + n_{off}$ the total number of NDC80 per kinetochore. Solving for the steady state gives:

$$f_{bound} \equiv \frac{n_{on}}{n} = (1 + K_{binding})^{-1} \quad (\text{Eq. 4})$$

3 where $K_{binding} = k_{off}/k_{on}$ is the equilibrium constant for the NDC80 binding, and f_{bound} is the NDC80
 4 binding fraction.

5
 6 The binding affinity of NDC80 decreases with the phosphorylation level of NDC80 (Figure 4) (Zaytsev et
 7 al., 2015), arguing that $K_{binding}$ is a function of f_{phos} . Since f_{phos} is small in late prometaphase and
 8 metaphase ($< 1/9$), we approximate the function by a first-order polynomial, i.e., $K_{binding}(f_{phos}) \approx K_0 +$
 9 $K'_0 f_{phos}$, and consequently Eq. 4 becomes:

$$f_{bound} = (1 + K_0 + K'_0 f_{phos})^{-1} \quad (\text{Eq. 5})$$

10 Combining Eq. 3 and 5, we have the relationship between the total Aurora B concentration $[A]$ and the
 11 NDC80 binding fraction f_{bound} as:

$$f_{bound} = \begin{cases} \left(1 + K_0 + K'_0 \left(1 + \frac{K_{phos}}{A^* - K}\right)^{-1}\right)^{-1}, & [A] < A^* \\ \left(1 + K_0 + K'_0 \left(1 + \frac{K_{phos}}{[A] - K}\right)^{-1}\right)^{-1}, & [A] \geq A^* \end{cases} \quad (\text{Eq. 6})$$

12
 13 We first determined the parameters K_0 and K'_0 by fitting Eq. 5 to the NDC80 binding fraction vs.
 14 phosphorylation level data in Figure 4C, which yielded $K_0 = 1.43 \pm 0.06$ (SE) and $K'_0 = 18 \pm 2$ (SE).
 15 To estimate the remaining three free parameters, K , K_{phos} , and A^* , we fit Eq. 6 to the NDC80 binding
 16 fraction vs. Aurora B concentration at NDC80 data (Figure 7), and obtained $K = 3.5 \pm 0.4$ μM (SE),
 17 $K_{phos} = 19 \pm 5$ μM (SE), and $A^* = 4.7 \pm 0.2$ μM (SE).

1

2 **Supplemental experiments**

3 Measurement of the fraction of β -tubulin labeled with TC-FIAsH

4 To measure the fraction of β -tubulin labeled with TC-FIAsH, we sought to determine the concentration of
5 labeled β -tubulin in the cell, and divide it by the total concentration of β -tubulin. We calculated the
6 concentration of labeled β -tubulin by combining 3D fluorescence microscopy to measure the total
7 fluorescence of β -tubulin-TC-FIAsH per cell, and fluorescence correlation spectroscopy (FCS) to measure
8 the fluorescence per molecule of TC-FIAsH.

9

10 *3D fluorescence microscopy:* We acquired z-stacks of β -tubulin-TC-FIAsH in mitotic cells using two-
11 photon fluorescence microscopy (Figure S8A), and then segmented the 3D images using an active
12 contour approach (Figure S8B). Assuming that the cytoplasmic background results from FIAsH binding
13 specifically to monomeric β -tubulin and nonspecifically to cysteine-rich proteins freely diffusing in the
14 cytoplasm, the average number of photons emitted from β -tubulin-TC-FIAsH in microtubules is the
15 difference between the average photon rate throughout the entire cell ($423 \pm 33 \text{ ms}^{-1}$) and the average
16 photon rate in the cytoplasm (determined from the mode of fluorescence distribution within each
17 segmented image, $327 \pm 30 \text{ ms}^{-1}$), which is $96 \pm 12 \text{ ms}^{-1}$ (Figure S8C). The instrumental setting of two-
18 photon fluorescence microscopy was identical to that of the FLIM system described above, where the
19 imaging parameters are: laser wavelength, 865 nm; excitation intensity, 3 mW; integration time, 3
20 seconds; z-stack separation, 0.5 μm ; scanning area, 27.5 $\mu\text{m} \times 27.5 \mu\text{m}$.

21

22 *Fluorescence correlation spectroscopy:* To convert the measured photon rate from fluorescence
23 microscopy to a measurement of the absolute concentration of β -tubulin-TC-FIAsH, we used two-photon
24 FCS to determine the volume of the point spread function (PSF) and the molecular brightness (i.e. the
25 number of photons emitted per molecule per second) of TC-FIAsH (Hess and Webb, 2002).

1 First, we performed an FCS measurement on 97-nM Alexa Fluor 488 (Thermo Fisher) in water.
2 FCS measurements were performed on the same instrumental setting as the 3D fluorescence microscopy
3 described above, with laser intensity 5 mW. 5 autocorrelation functions, each of which had been collected
4 for 300 seconds, were averaged, and then the following FCS model, $G_D(\tau)$, was fitted to the average
5 autocorrelation function:

$$G_D(\tau) = \frac{1}{V_{eff}\chi^2 C} \left(\frac{1}{1 + 8D\tau/w_{xy}^2} \right) \left(\frac{1}{1 + 8D\tau/w_z^2} \right)^{\frac{1}{2}} + G_{\infty}$$

6 where V_{eff} is the effective volume of PSF, C the concentration of fluorophores (which is 97 nM), χ^2 the
7 background noise correction factor (Hess and Webb, 2002), D the diffusion coefficient of Alexa Fluor
8 488, which was previously estimated to be 435 $\mu\text{m}^2/\text{s}$ (Petrasek and Schwille, 2008), and w_{xy} and w_z are
9 the radial and axial beam waists, respectively (Figure S8D). w_z can be written in terms of V_{eff} and w_{xy} :

$$w_z = \left(\frac{2}{\pi} \right)^{3/2} \frac{V_{eff}}{w_{xy}^2}$$

10 Fitting the FCS model to the Alexa 488 FCS data estimated V_{eff} and w_{xy} to be $0.364 \pm 0.004 \mu\text{m}^3$ and 278
11 ± 4 nm, respectively (Figure S8D).

12 We next performed an FCS measurement on a synthesized TC peptide labeled with FIAsh. 50
13 μM synthesized TC peptide (Ac-AEEEEACCPGCC-NH₂, Genscript), 100 μM FIAsh-EDT₂, and 10 mM
14 2-mercaptoethanesulfonate (Sigma Aldrich) were incubated for an hour to associate TC peptide with
15 FIAsh, then diluted in the imaging buffer by 500 times, and prepared on a coverslip for FCS
16 measurement. The laser intensity was set to 3 mW. 6 autocorrelation functions, each of which had been
17 collected for 300 seconds, were averaged, and the following FCS model was fitted to the average
18 autocorrelation function to determine the number of fluorophores N in a focal volume V_{eff} :

$$G_D(\tau) = \frac{1}{N\chi^2} \left(\frac{1}{1 + \tau/\tau_D} \right) \left(\frac{1}{1 + (w_{xy}^2/w_z^2)(\tau/\tau_D)} \right)^{\frac{1}{2}} + G_{\infty}$$

1 while w_{xy} and w_z were fixed to the values determined from the FCS measurement on Alexa Fluor 488
2 (Figure S8E). The photon count collected during the FCS measurement was corrected for background
3 noise, and then divided by N to yield the molecular brightness of TC-FIAsH, $233.4 \pm 9.3 \text{ s}^{-1}$. Using the
4 estimated molecular brightness and the effective volume of the PSF, we calculated the average
5 concentration of the polymerized β -tubulin-TC-FIAsH to be

$$\frac{9.6 \times 10^4 \text{ s}^{-1}}{(233.4 \text{ s}^{-1})(0.364 \mu\text{m}^3)} = 1.13 \times 10^{21} \text{ m}^{-3} = 1.88 \pm 0.13 \mu\text{M}$$

6
7 *Calculating labeling ratio:* A previous study (Dumontet et al., 1996) estimated the percentage of
8 polymerized β -tubulin in a mitotic human tissue culture cell to be $36\% \pm 7\%$. Combining this information
9 with our estimate of an average concentration of polymerized β -tubulin-TC-FIAsH of $1.88 \pm 0.13 \mu\text{M}$
10 leads to a total concentration of β -tubulin-TC-FIAsH of $1.88 \mu\text{M} \times 100/36 \approx 5.22 \pm 1.08 \mu\text{M}$. Since the
11 total concentration of tubulin dimer in a tissue culture cell is $\sim 20 \mu\text{M}$ (Hiller and Weber, 1978), we
12 estimated the fraction of labeled β -tubulin to be $5.22 \mu\text{M}/20 \mu\text{M} \approx 26.1\% \pm 5.4\%$.

13
14 Förster radius estimation

15 To measure the Förster radius R_0 of FRET between mTurquoise2 and TC-FIAsH, we created a construct
16 containing mTurquoise2 tethered to TC (mTurquoise2-TC), expressed it in U2OS cells, and acquired
17 fluorescence decays of mTurquoise2 using FLIM, which were well-described by a single-exponential
18 fluorescence decay with a lifetime of $3.75 \text{ ns} \pm 0.03 \text{ ns}$ (SD) in the absence of FIAsH labeling (Figure
19 S3A). When FIAsH is added to these cells, FLIM measurements revealed the presence of additional
20 shorter-lifetime species, corresponding to mTurquoise2 molecules engaged in FRET with TC-FIAsH
21 (Figure S3A). Then we performed Monte Carlo protein simulations (which are described below) to model
22 the conformational ensemble of the flexible tether between mTurquoise2 and TC-FIAsH and obtain the

1 distribution $p(r)$ of the distance r between mTurquoise2 and FIAsh (Figure S3B). The fluorescence
2 lifetime τ of donors engaged in FRET is related to the donor-acceptor distance r by:

$$\tau(r; R_0) = \frac{\tau_D}{1 + \left(\frac{R_0}{r}\right)^6}$$

3 where τ_D is the fluorescence lifetime of the donor in non-FRET state ($3.75 \text{ ns} \pm 0.03 \text{ ns}$), and R_0 is the
4 Förster radius. Therefore, the fluorescence decay $y(t)$ of mTurquoise2-TC-FIAsh can be modeled as:

$$y(t) = A_D \exp\left(-\frac{t}{\tau_D}\right) + A_{\text{FRET}} \int p(r) \exp\left(-\frac{t}{\tau(r; R_0)}\right) dr$$

5 where A_D is the population in the non-FRET state and A_{FRET} is that in the FRET state, both of which are
6 free parameters of the model along with R_0 . This model (after convolved with the IRF) was fit to the
7 measured fluorescence decay curve of mTurquoise2-TC-FIAsh, allowing us to estimate the Förster radius
8 R_0 to be $5.90 \text{ nm} \pm 0.10 \text{ nm}$ (Figure S3C).

9

10 Characterization and calibration of NDC80-kMT FLIM-FRET measurements by Monte Carlo simulations

11 *Characterization of NDC80-kMT FRET vs NDC80-MT distance relationship:* To characterize the FRET
12 between mTurquoise2-NDC80 and FIAsh-labeled microtubule when NDC80 is not bound to the
13 microtubule, we performed large-scale, atomistic Monte Carlo protein simulations to model the
14 conformational ensemble of the tether between mTurquoise2 and NDC80 and the disordered C-terminal
15 tails of twelve β -tubulins near the NDC80 complex (which is described below) (Figure S4A). 4000 sets of
16 positions of mTurquoise2 and TC were generated for each case where the NDC80 bound to an inter- or
17 intra-tubulin dimer interface was translated away from the microtubule by a certain distance (0~15 nm,
18 0.5 nm increment) in a direction perpendicular to the microtubule surface. For each randomly sampled set
19 of distances between mTurquoise2 and TC-FIAsh, $\vec{r} = \{r_i\}$, the fluorescence lifetime was calculated by:

$$\tau(\vec{r}) = \frac{\tau_D}{1 + \sum_{i=1}^{12} I_i \left(\frac{R_0}{r_i}\right)^6}$$

1 where $I_i \sim \text{Bernoulli}(f_{label})$ indicates whether or not the i -th TC motif is labeled with FLaSH-EDT₂; R_0 is
2 the Förster radius between mTurquoise2 and TC-FlAsH; and $\tau_D = 3.75$ ns is the non-FRET lifetime of
3 mTurquoise2 (Figure S4A). The estimated labeling fraction 26.1% and the Förster radius 5.90 nm were
4 used for f_{label} and R_0 , respectively. For each NDC80-kMT distance, 2 million fluorescence lifetimes
5 were sampled, based on which we simulated 30 fluorescence decay curves of mTurquoise2 by:

$$\text{Poisson} \left(A \int p(\vec{r}) \exp \left(-\frac{t}{\tau(\vec{r})} \right) d\vec{r} \right)$$

6 where the amplitude A of the fluorescence decay was set to 5000 (Figure S4A). Single- and double-
7 exponential decay models were fit to the simulated fluorescence decays (by maximum likelihood method)
8 (Figure S4B, bottom). The Bayesian information criterion (BIC) was used as a criterion for model
9 selection between the single- and double-exponential decay models. The difference in BIC between
10 single- and double-exponential models, $\Delta\text{BIC} = \text{BIC}_{1\text{expo}} - \text{BIC}_{2\text{expo}}$, was plotted against the NDC80-
11 kMT distance (Figure S4B, top right). ΔBIC is negative when NDC80-kMT distance is larger than 8 nm,
12 indicating that single-exponential model performs better than double-exponential model in terms of the
13 goodness of fit and the complexity of model (Figure S4B).

14
15 *NDC80-kMT FRET fraction calibration:* To obtain the relationship between NDC80 FRET fraction and
16 NDC80 binding fraction, we performed large-scale Monte Carlo simulations to obtain 4000 sets of
17 distances between mTurquoise2 and TC-FlAsH, $\vec{r} = \{r_i\}$, for each case where mTurquoise2-NDC80 is
18 bound to the TC-tagged microtubule at the inter- or intra-dimer interface. Then we sampled 0.5 million
19 fluorescence lifetimes τ as described above, and simulated a fluorescence decay curve for the situation
20 where a fraction f_b of mTurquoise2-NDC80 are bound to microtubules and have lifetime $\tau(\vec{r})$, while the
21 other $1 - f_b$ are not bound and have lifetime τ_D (Figure 4C, green dots):

$$\text{Poisson} \left(A \left[(1 - f_b) \exp \left(-\frac{t}{\tau_D} \right) + f_b \int p(\vec{r}) \exp \left(-\frac{t}{\tau(\vec{r})} \right) d\vec{r} \right] \right)$$

1 where the amplitude A of the fluorescence decay curve was set to 10,000 (Figure S4C, left). The
2 simulated fluorescence decay curve was then fit by two-exponential fluorescence decay model (Figure
3 S4C, red lines):

$$A' \left[(1 - f_{FRET}) \exp\left(-\frac{t}{\tau_D}\right) + f_{FRET} \exp\left(-\frac{t}{\tau_{FRET}}\right) \right]$$

4 to acquire the FRET fraction, f_{FRET} . The data of NDC80 FRET fraction, f_{FRET} , vs NDC80 binding
5 fraction, f_b , was fit using a linear model $f_{FRET} = a f_b$ (Figure S4C, right). To determine the uncertainty in
6 the slope a (gray area in Figure S4C, right), we repeated the process above with the mean \pm error values
7 of R_0 and beta-tubulin labeling fraction f_{label} . As a result, we obtained $a = 0.42 \pm 0.08$, and used this
8 calibration to convert NDC80 FRET fraction to NDC80 binding fraction.

9

10 Monte Carlo protein simulations

11 Atomistic simulations were performed by the CAMPARI (v2) package (Vitalis and Pappu, 2009b),
12 employing the ABSINTH implicit solvation model and forcefield paradigm (Vitalis and Pappu, 2009a) at
13 the intrinsic solvation (IS) limit (Das and Pappu, 2013) (unless stated otherwise), where the energy
14 function is simply a combination of Lennard-Jones energy and ABSINTH solvation energy.

15

16 *mTurquoise2-TC construct simulation:* For the Förster radius estimation, we ran 50 independent
17 simulations on the mTurquoise2-TC construct in spherical soft-wall boundary conditions with radius 100
18 Å. An input structure was used only for the folded mTurquoise2 domain (adapted from PDB 4B5Y), and
19 we employed CAMPARI to generate the tether and TC domains (GMDELYKYSDLFLNCCPGCCMEP)
20 from scratch. To prevent unphysical unfolding and/or conformational change of mTurquoise2, we
21 imposed constraints on internal degrees of freedom of residues in the folded region. Each simulation
22 consisted of 2×10^6 MC steps with sampling frequency of $(5,000 \text{ steps})^{-1}$, and the simulation temperature
23 was set to 400 K in order to scan a large structural ensemble. Note that the system is quickly relaxed in

1 the intrinsic solvation (IS) limit, and hence it does not require a long simulation time to reach
2 equilibration. The average coordinate of the alpha carbons of 4 residues before and after Trp66 was used
3 as the location of mTurquoise2 chromophore, and the average coordinate of alpha carbons of the four
4 cysteine residues in the TC motif was used as the location of TC-FIAsH.

5
6 *mTurquoise2-NDC80 and TC-labeled microtubule simulation:* We constructed a system consisting of the
7 NDC80 complex, 12 tubulin dimers as described in Figure S4A. The initial structures of the system were
8 constructed by combining the structures of microtubule (PDB 3JAS) (Zhang et al., 2015) and one of
9 bonsai-NDC80s attached to a tubulin dimer at the inter- and intra-dimer interfaces (PDB 3IZ0) (Alushin
10 et al., 2010), and then incorporating the structures of disordered regions (tether, GMDEL YKYS DLMET,
11 and C-terminal tail+TC, SEYQQ YQDAT AEEEE DFGEE AEEEA CCPGC C) generated by the loop
12 modeling module of Rosetta 3.8 (Mandell et al., 2009, Leaver-Fay et al., 2011). Clashes in the initial
13 structure were removed by the Rosetta relaxation module (Nivón et al., 2013). For folded regions (where
14 we have structure information from PDB), we imposed constraints on internal degrees of freedom as
15 before. To prevent dissociation of microtubule into individual tubulins, we also imposed a harmonic
16 restraint potential on atoms at the interface of two different chains. If two atoms from different chains are
17 closer than 20 Å, the pair contributes an additional potential

$$E_{\text{drest}}(i, j) = k(r_{ij} - r_{ij}^0)^2,$$

18 where i and j are atomic indices, r_{ij} is the distance between two atoms i and j , r_{ij}^0 is the initial distance
19 between i and j , and k is a force constant (set to 3.0 kcal/mol/Å²). We employed spherical soft-wall
20 boundary conditions with radius 200 Å, and the simulation temperature of 400 K. We ran a relaxation
21 simulation for 2×10^6 MC steps, and a production simulation for another 2×10^6 MC steps with sampling
22 frequency of (500 steps)⁻¹. For the FRET efficiency vs NDC80-MT data (Figure S4B), we used the final
23 structure of the relaxation simulation and translated the NDC80 complex along the axis orthogonal to the

1 microtubule surface by several distance values: from 0 to 15 nm by increment of 0.5 nm. For each system,
2 a simulation of 2×10^6 MC steps was conducted to generate data with sampling frequency of $(500 \text{ steps})^{-1}$.

3

4 **Protein structure illustration**

5 Protein structure illustrations were generated by The PyMOL Molecular Graphics System, Version 2.0
6 Schrödinger, LLC.

7

8 **Quantification and Statistical Analysis**

9 The statistical test used, sample size (number of cells and kinetochores), dispersion and precision
10 measures can be found in figure legends, Results, or below. Linear and exponential fitting presented in
11 Figure 2D, 3D, 4A, 4B, 5C, 6D, 7A, S5A, and S6D were performed by Levenberg-Marquardt algorithm
12 with residuals weighted by the inverse of y-errors, and the corresponding 95% confidence intervals were
13 calculated by *predint* function in MATLAB. To assess the significance of correlation, we determined p-
14 value from $1 - \alpha$, where α is the smallest confidence level that makes zero contained in the confidence
15 interval of the slope of the linear fit.

ACKNOWLEDGMENTS

We thank A. Murray and N. Kleckner for comments on the manuscript; J. DeLuca, M. Lampson, and I. Cheeseman for reagents; F. Rago for help with retroviral transfection; D. Kim for help with nucleofection; Needleman lab members and J. Oh for proof reading, comments and discussion. This work was supported by National Science Foundation grants DBI-0959721 and DMR-0820484, and the National Institutes of Health R01NS056114 (RVP). T.Y.Y. is supported by a Samsung Scholarship. The authors declare no competing financial interests.

COMPETING INTERESTS

The authors declare no competing financial interests.

AUTHOR CONTRIBUTIONS

Conceptualization, T.Y.Y. and D.J.N.; Methodology, T.Y.Y. and C.Y.; Software, T.Y.Y. and J.-M.C.; Formal Analysis, T.Y.Y. and J.-M.C.; Investigation, T.Y.Y. and J.-M.C.; Writing – Original Draft, T.Y.Y. and D.J.N.; Writing – Review & Editing, T.Y.Y., J.-M.C., C.Y., R.V.P., and D.J.N.; Visualization, T.Y.Y.; Supervision, R.V.P. and D.J.N.; Funding Acquisition, R.V.P. and D.J.N.

REFERENCES

- AKIYOSHI, B., SARANGAPANI, K. K., POWERS, A. F., NELSON, C. R., REICHOW, S. L., ARELLANO-SANTOYO, H., GONEN, T., RANISH, J. A., ASBURY, C. L. & BIGGINS, S. 2010. Tension directly stabilizes reconstituted kinetochore-microtubule attachments. *Nature*, 468, 576-9.
- ALUSHIN, G. M., RAMEY, V. H., PASQUALATO, S., BALL, D. A., GRIGORIEFF, N., MUSACCHIO, A. & NOGALES, E. 2010. The Ndc80 kinetochore complex forms oligomeric arrays along microtubules. *Nature*, 467, 805-10.
- ANDRESEN, M., SCHMITZ-SALUE, R. & JAKOBS, S. 2004. Short tetracysteine tags to beta-tubulin demonstrate the significance of small labels for live cell imaging. *Mol Biol Cell*, 15, 5616-22.

- ARMOND, J. W., VLADIMIROU, E., ERENT, M., MCAINSH, A. D. & BURROUGHS, N. J. 2015. Probing microtubule polymerisation state at single kinetochores during metaphase chromosome motion. *J Cell Sci*, 128, 1991-2001.
- BEREZIN, M. Y. & ACHILEFU, S. 2010. Fluorescence lifetime measurements and biological imaging. *Chem Rev*, 110, 2641-84.
- BIGGINS, S., SEVERIN, F. F., BHALLA, N., SASSOON, I., HYMAN, A. A. & MURRAY, A. W. 1999. The conserved protein kinase Ipl1 regulates microtubule binding to kinetochores in budding yeast. *Genes Dev*, 13, 532-44.
- BISHOP, J. D. & SCHUMACHER, J. M. 2002. Phosphorylation of the carboxyl terminus of inner centromere protein (INCENP) by the Aurora B Kinase stimulates Aurora B kinase activity. *J Biol Chem*, 277, 27577-80.
- CAMPBELL, C. S. & DESAI, A. 2013. Tension sensing by Aurora B kinase is independent of survivin-based centromere localization. *Nature*, 497, 118-21.
- CARMENA, M., WHEELLOCK, M., FUNABIKI, H. & EARNSHAW, W. C. 2012. The chromosomal passenger complex (CPC): from easy rider to the godfather of mitosis. *Nat Rev Mol Cell Biol*, 13, 789-803.
- CHEESEMAN, I. M., CHAPPIE, J. S., WILSON-KUBALEK, E. M. & DESAI, A. 2006. The conserved KMN network constitutes the core microtubule-binding site of the kinetochore. *Cell*, 127, 983-97.
- CHEESEMAN, I. M. & DESAI, A. 2008. Molecular architecture of the kinetochore-microtubule interface. *Nat Rev Mol Cell Biol*, 9, 33-46.
- CIFERRI, C., PASQUALATO, S., SCREPANTI, E., VARETTI, G., SANTAGUIDA, S., DOS REIS, G., MAIOLICA, A., POLKA, J., DE LUCA, J. G., DE WULF, P., SALEK, M., RAPPSILBER, J., MOORES, C. A., SALMON, E. D. & MUSACCHIO, A. 2008. Implications for kinetochore-microtubule attachment from the structure of an engineered Ndc80 complex. *Cell*, 133, 427-39.
- CIMINI, D., WAN, X., HIREL, C. B. & SALMON, E. D. 2006. Aurora kinase promotes turnover of kinetochore microtubules to reduce chromosome segregation errors. *Curr Biol*, 16, 1711-8.
- DAS, R. K. & PAPPU, R. V. 2013. Conformations of intrinsically disordered proteins are influenced by linear sequence distributions of oppositely charged residues. *Proceedings of the National Academy of Sciences*, 110, 13392-13397.
- DELUCA, J. G., GALL, W. E., CIFERRI, C., CIMINI, D., MUSACCHIO, A. & SALMON, E. D. 2006. Kinetochore microtubule dynamics and attachment stability are regulated by Hec1. *Cell*, 127, 969-82.
- DUMONTET, C., DURAN, G. E., STEGER, K. A., MURPHY, G. L., SUSSMAN, H. H. & SIKIC, B. I. 1996. Differential expression of tubulin isoforms during the cell cycle. *Cell Motil Cytoskeleton*, 35, 49-58.
- EDELSTEIN, A. D., TSUCHIDA, M. A., AMODAJ, N., PINKARD, H., VALE, R. D. & STUURMAN, N. 2014. Advanced methods of microscope control using muManager software. *J Biol Methods*, 1.

- FULLER, B. G., LAMPSON, M. A., FOLEY, E. A., ROSASCO-NITCHER, S., LE, K. V., TOBELMANN, P., BRAUTIGAN, D. L., STUKENBERG, P. T. & KAPOOR, T. M. 2008. Midzone activation of aurora B in anaphase produces an intracellular phosphorylation gradient. *Nature*, 453, 1132-6.
- GODEK, K. M., KABECHE, L. & COMPTON, D. A. 2015. Regulation of kinetochore-microtubule attachments through homeostatic control during mitosis. *Nat Rev Mol Cell Biol*, 16, 57-64.
- GOEDHART, J., VON STETTEN, D., NOIRCLERC-SAVOYE, M., LELIMOUSIN, M., JOOSEN, L., HINK, M. A., VAN WEEREN, L., GADELLA, T. W., JR. & ROYANT, A. 2012. Structure-guided evolution of cyan fluorescent proteins towards a quantum yield of 93%. *Nat Commun*, 3, 751.
- GUIMARAES, G. J., DONG, Y., MCEWEN, B. F. & DELUCA, J. G. 2008. Kinetochore-microtubule attachment relies on the disordered N-terminal tail domain of Hec1. *Curr Biol*, 18, 1778-84.
- HAASE, J., BONNER, M. K., HALAS, H. & KELLY, A. E. 2017. Distinct Roles of the Chromosomal Passenger Complex in the Detection of and Response to Errors in Kinetochore-Microtubule Attachment. *Dev Cell*, 42, 640-654 e5.
- HAUF, S., COLE, R. W., LATERRA, S., ZIMMER, C., SCHNAPP, G., WALTER, R., HECKEL, A., VAN MEEL, J., RIEDER, C. L. & PETERS, J. M. 2003. The small molecule Hesperadin reveals a role for Aurora B in correcting kinetochore-microtubule attachment and in maintaining the spindle assembly checkpoint. *J Cell Biol*, 161, 281-94.
- HESS, S. T. & WEBB, W. W. 2002. Focal volume optics and experimental artifacts in confocal fluorescence correlation spectroscopy. *Biophys J*, 83, 2300-17.
- HILLER, G. & WEBER, K. 1978. Radioimmunoassay for tubulin: a quantitative comparison of the tubulin content of different established tissue culture cells and tissues. *Cell*, 14, 795-804.
- HOFFMANN, C., GAIETTA, G., BUNEMANN, M., ADAMS, S. R., OBERDORFF-MAASS, S., BEHR, B., VILARDAGA, J. P., TSIEN, R. Y., ELLISMAN, M. H. & LOHSE, M. J. 2005. A FIAsh-based FRET approach to determine G protein-coupled receptor activation in living cells. *Nat Methods*, 2, 171-6.
- HOFFMANN, C., GAIETTA, G., ZURN, A., ADAMS, S. R., TERRILLON, S., ELLISMAN, M. H., TSIEN, R. Y. & LOHSE, M. J. 2010. Fluorescent labeling of tetracysteine-tagged proteins in intact cells. *Nat Protoc*, 5, 1666-77.
- HUANG, H. B., HORIUCHI, A., GOLDBERG, J., GREENGARD, P. & NAIRN, A. C. 1997. Site-directed mutagenesis of amino acid residues of protein phosphatase 1 involved in catalysis and inhibitor binding. *Proc Natl Acad Sci U S A*, 94, 3530-5.
- KABECHE, L. & COMPTON, D. A. 2013. Cyclin A regulates kinetochore microtubules to promote faithful chromosome segregation. *Nature*, 502, 110-3.
- KAYE, B., FOSTER, P. J., YOO, T. Y. & NEEDLEMAN, D. J. 2017. Developing and Testing a Bayesian Analysis of Fluorescence Lifetime Measurements. *PLoS One*, 12, e0169337.

- KELLY, A. E., SAMPATH, S. C., MANIAR, T. A., WOO, E. M., CHAIT, B. T. & FUNABIKI, H. 2007. Chromosomal enrichment and activation of the aurora B pathway are coupled to spatially regulate spindle assembly. *Dev Cell*, 12, 31-43.
- LAMPSON, M. A. & CHEESEMAN, I. M. 2011. Sensing centromere tension: Aurora B and the regulation of kinetochore function. *Trends Cell Biol*, 21, 133-40.
- LEANDRO-GARCIA, L. J., LESKELA, S., LANDA, I., MONTERO-CONDE, C., LOPEZ-JIMENEZ, E., LETON, R., CASCON, A., ROBLEDO, M. & RODRIGUEZ-ANTONA, C. 2010. Tumoral and tissue-specific expression of the major human beta-tubulin isoforms. *Cytoskeleton (Hoboken)*, 67, 214-23.
- LEAVER-FAY, A., TYKA, M., LEWIS, S. M., LANGE, O. F., THOMPSON, J., JACAK, R., KAUFMAN, K. W., RENFREW, P. D., SMITH, C. A., SHEFFLER, W., DAVIS, I. W., COOPER, S., TREUILLE, A., MANDELL, D. J., RICHTER, F., BAN, Y.-E. A., FLEISHMAN, S. J., CORN, J. E., KIM, D. E., LYSKOV, S., BERRONDO, M., MENTZER, S., POPOVIĆ, Z., HAVRANEK, J. J., KARANICOLAS, J., DAS, R., MEILER, J., KORTEMME, T., GRAY, J. J., KUHLMAN, B., BAKER, D. & BRADLEY, P. 2011. Chapter nineteen - Rosetta3: An Object-Oriented Software Suite for the Simulation and Design of Macromolecules. *In*: JOHNSON, M. L. & BRAND, L. (eds.) *Methods in Enzymology*. Academic Press.
- LIU, D., VADER, G., VROMANS, M. J., LAMPSON, M. A. & LENS, S. M. 2009. Sensing chromosome bi-orientation by spatial separation of aurora B kinase from kinetochore substrates. *Science*, 323, 1350-3.
- MAGIDSON, V., O'CONNELL, C. B., LONCAREK, J., PAUL, R., MOGILNER, A. & KHODJAKOV, A. 2011. The spatial arrangement of chromosomes during prometaphase facilitates spindle assembly. *Cell*, 146, 555-67.
- MAIATO, H., DELUCA, J., SALMON, E. D. & EARNSHAW, W. C. 2004. The dynamic kinetochore-microtubule interface. *J Cell Sci*, 117, 5461-77.
- MANDELL, D. J., COUTSIAS, E. A. & KORTEMME, T. 2009. Sub-angstrom accuracy in protein loop reconstruction by robotics-inspired conformational sampling. *Nat Meth*, 6, 551-552.
- NICKLAS, R. B. & KOCH, C. A. 1969. Chromosome micromanipulation. 3. Spindle fiber tension and the reorientation of mal-oriented chromosomes. *J Cell Biol*, 43, 40-50.
- NICKLAS, R. B. & WARD, S. C. 1994. Elements of error correction in mitosis: microtubule capture, release, and tension. *J Cell Biol*, 126, 1241-53.
- NIVÓN, L. G., MORETTI, R. & BAKER, D. 2013. A Pareto-Optimal Refinement Method for Protein Design Scaffolds. *PLOS ONE*, 8, e59004.
- PELLETIER, V., GAL, N., FOURNIER, P. & KILFOIL, M. L. 2009. Microrheology of microtubule solutions and actin-microtubule composite networks. *Phys Rev Lett*, 102, 188303.
- PETRASEK, Z. & SCHWILLE, P. 2008. Precise measurement of diffusion coefficients using scanning fluorescence correlation spectroscopy. *Biophys J*, 94, 1437-48.

- POSCH, M., KHOUDOLI, G. A., SWIFT, S., KING, E. M., DELUCA, J. G. & SWEDLOW, J. R. 2010. Sds22 regulates aurora B activity and microtubule-kinetochore interactions at mitosis. *J Cell Biol*, 191, 61-74.
- RAN, F. A., HSU, P. D., WRIGHT, J., AGARWALA, V., SCOTT, D. A. & ZHANG, F. 2013. Genome engineering using the CRISPR-Cas9 system. *Nat Protoc*, 8, 2281-2308.
- RIEDER, C. L. 1982. The formation, structure, and composition of the mammalian kinetochore and kinetochore fiber. *Int Rev Cytol*, 79, 1-58.
- ROSASCO-NITCHER, S. E., LAN, W., KHORASANIZADEH, S. & STUKENBERG, P. T. 2008. Centromeric Aurora-B activation requires TD-60, microtubules, and substrate priming phosphorylation. *Science*, 319, 469-72.
- ROWLEY, M. I., COOLEN, A. C., VOJNOVIC, B. & BARBER, P. R. 2016. Robust Bayesian Fluorescence Lifetime Estimation, Decay Model Selection and Instrument Response Determination for Low-Intensity FLIM Imaging. *PLoS One*, 11, e0158404.
- SALIMIAN, K. J., BALLISTER, E. R., SMOAK, E. M., WOOD, S., PANCHENKO, T., LAMPSON, M. A. & BLACK, B. E. 2011. Feedback control in sensing chromosome biorientation by the Aurora B kinase. *Curr Biol*, 21, 1158-65.
- SANTAGUIDA, S. & AMON, A. 2015. Short- and long-term effects of chromosome mis-segregation and aneuploidy. *Nat Rev Mol Cell Biol*, 16, 473-85.
- SESSA, F., MAPELLI, M., CIFERRI, C., TARRICONE, C., ARECES, L. B., SCHNEIDER, T. R., STUKENBERG, P. T. & MUSACCHIO, A. 2005. Mechanism of Aurora B activation by INCENP and inhibition by hesperadin. *Mol Cell*, 18, 379-91.
- SHANER, N. C., LAMBERT, G. G., CHAMMAS, A., NI, Y., CRANFILL, P. J., BAIRD, M. A., SELL, B. R., ALLEN, J. R., DAY, R. N., ISRAELSSON, M., DAVIDSON, M. W. & WANG, J. 2013. A bright monomeric green fluorescent protein derived from Branchiostoma lanceolatum. *Nat Methods*, 10, 407-9.
- SUZUKI, A., BADGER, B. L. & SALMON, E. D. 2015. A quantitative description of Ndc80 complex linkage to human kinetochores. *Nat Commun*, 6, 8161.
- TANAKA, T. U., RACHIDI, N., JANKE, C., PEREIRA, G., GALOVA, M., SCHIEBEL, E., STARK, M. J. & NASMYTH, K. 2002. Evidence that the Ipl1-Sli15 (Aurora kinase-INCENP) complex promotes chromosome bi-orientation by altering kinetochore-spindle pole connections. *Cell*, 108, 317-29.
- TAUCHMAN, E. C., BOEHM, F. J. & DELUCA, J. G. 2015. Stable kinetochore-microtubule attachment is sufficient to silence the spindle assembly checkpoint in human cells. *Nat Commun*, 6, 10036.
- THURBER, G. M., REINER, T., YANG, K. S., KOHLER, R. H. & WEISSLEDER, R. 2014. Effect of small-molecule modification on single-cell pharmacokinetics of PARP inhibitors. *Mol Cancer Ther*, 13, 986-95.

- TIRNAUER, J. S., CANMAN, J. C., SALMON, E. D. & MITCHISON, T. J. 2002. EB1 targets to kinetochores with attached, polymerizing microtubules. *Mol Biol Cell*, 13, 4308-16.
- VITALIS, A. & PAPPU, R. V. 2009a. ABSINTH: A new continuum solvation model for simulations of polypeptides in aqueous solutions. *Journal of Computational Chemistry*, 30, 673-699.
- VITALIS, A. & PAPPU, R. V. 2009b. Chapter 3 Methods for Monte Carlo Simulations of Biomacromolecules. In: RALPH, A. W. (ed.) *Annual Reports in Computational Chemistry*. Elsevier.
- WANG, F., ULYANOVA, N. P., DAUM, J. R., PATNAIK, D., KATENEVA, A. V., GORBSKY, G. J. & HIGGINS, J. M. 2012. Haspin inhibitors reveal centromeric functions of Aurora B in chromosome segregation. *J Cell Biol*, 199, 251-68.
- XU, Z., VAGNARELLI, P., OGAWA, H., SAMEJIMA, K. & EARNSHAW, W. C. 2010. Gradient of increasing Aurora B kinase activity is required for cells to execute mitosis. *J Biol Chem*, 285, 40163-70.
- YOO, T. Y. & NEEDLEMAN, D. J. 2016. Studying Kinetochores In Vivo Using FLIM-FRET. *Methods Mol Biol*, 1413, 169-86.
- ZAYTSEV, A. V., MICK, J. E., MASLENNIKOV, E., NIKASHIN, B., DELUCA, J. G. & GRISHCHUK, E. L. 2015. Multisite phosphorylation of the NDC80 complex gradually tunes its microtubule-binding affinity. *Mol Biol Cell*, 26, 1829-44.
- ZAYTSEV, A. V., SEGURA-PENA, D., GODZI, M., CALDERON, A., BALLISTER, E. R., STAMATOV, R., MAYO, A. M., PETERSON, L., BLACK, B. E., ATAULLAKHANOV, F. I., LAMPSON, M. A. & GRISHCHUK, E. L. 2016. Bistability of a coupled Aurora B kinase-phosphatase system in cell division. *Elife*, 5, e10644.
- ZAYTSEV, A. V., SUNDIN, L. J., DELUCA, K. F., GRISHCHUK, E. L. & DELUCA, J. G. 2014. Accurate phosphoregulation of kinetochore-microtubule affinity requires unconstrained molecular interactions. *J Cell Biol*, 206, 45-59.
- ZHAI, Y., KRONEBUSCH, P. J. & BORISY, G. G. 1995. Kinetochore microtubule dynamics and the metaphase-anaphase transition. *J Cell Biol*, 131, 721-34.
- ZHANG, R., ALUSHIN, G. M., BROWN, A. & NOGALES, E. 2015. Mechanistic Origin of Microtubule Dynamic Instability and Its Modulation by EB Proteins. *Cell*, 162, 849-59.

SUPPLEMENTAL FIGURES

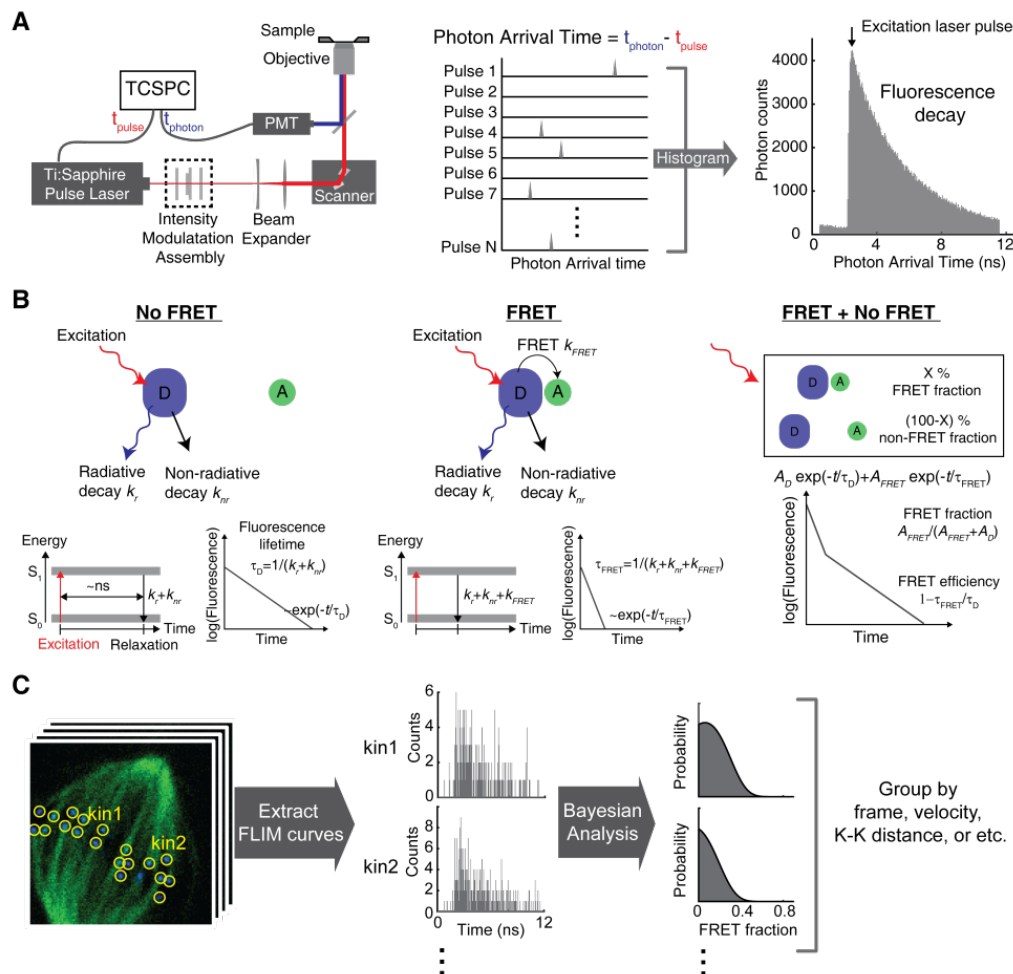


Figure S1. Kinetochores FLIM-FRET measurement

(A) Illustration of fluorescence decay acquisition in a TCSPC (time-correlated single photon counting) FLIM system. A Ti:Sapphire pulsed laser is used for excitation and a photomultiplier tube (PMT) for detection. The photon arrival time, the difference in timing between the emitted photon and excitation laser pulse, is measured by TCSPC, which is accumulated to a fluorescence decay curve over many laser repetition periods.

(B) The fluorescence lifetime is the average time the fluorophore stays in the excited state. (left) When the donor fluorophore (D) is not engaged in FRET with an acceptor (A) fluorophore, the donor fluorophore has a single-exponential fluorescence decay with fluorescence lifetime $\tau_D = 1/(k_r + k_{nr})$, where k_r and k_{nr} are the radiative and non-radiative decay rates, respectively. (middle) FRET provides an additional relaxation pathway to the excited donor, reducing the fluorescence lifetime of the donor to $\tau_{FRET} = 1/(k_r + k_{nr} + k_{FRET})$, where k_{FRET} is the FRET rate. (right) The fluorescence decay of a mixture of donors engaged in FRET and not engaged in FRET is a sum of two exponentials with two different lifetimes, τ_D and τ_{FRET} , which corresponds to the non-FRET and FRET populations, respectively. The relative amplitude of the short-lifetime exponential decay provides the fraction of the FRET population, and the lifetime ratio provides the intrinsic FRET efficiency.

(C) TCSPC FLIM provides fluorescence decay curve at each pixel, and the total photon counts in each pixel provides a two-photon fluorescence intensity image. To quantify the FRET fraction at each kinetochores, kinetochores were identified based on the intensity image, then the fluorescence decay

curves in the pixels within each kinetochore were summed. Then we performed a Bayesian analysis to obtain the posterior distribution of the FRET fraction at each kinetochore. The posterior distributions of the kinetochores in a group of kinetochores were combined by multiplication to compute the mean and SEM of the FRET fraction for the group.

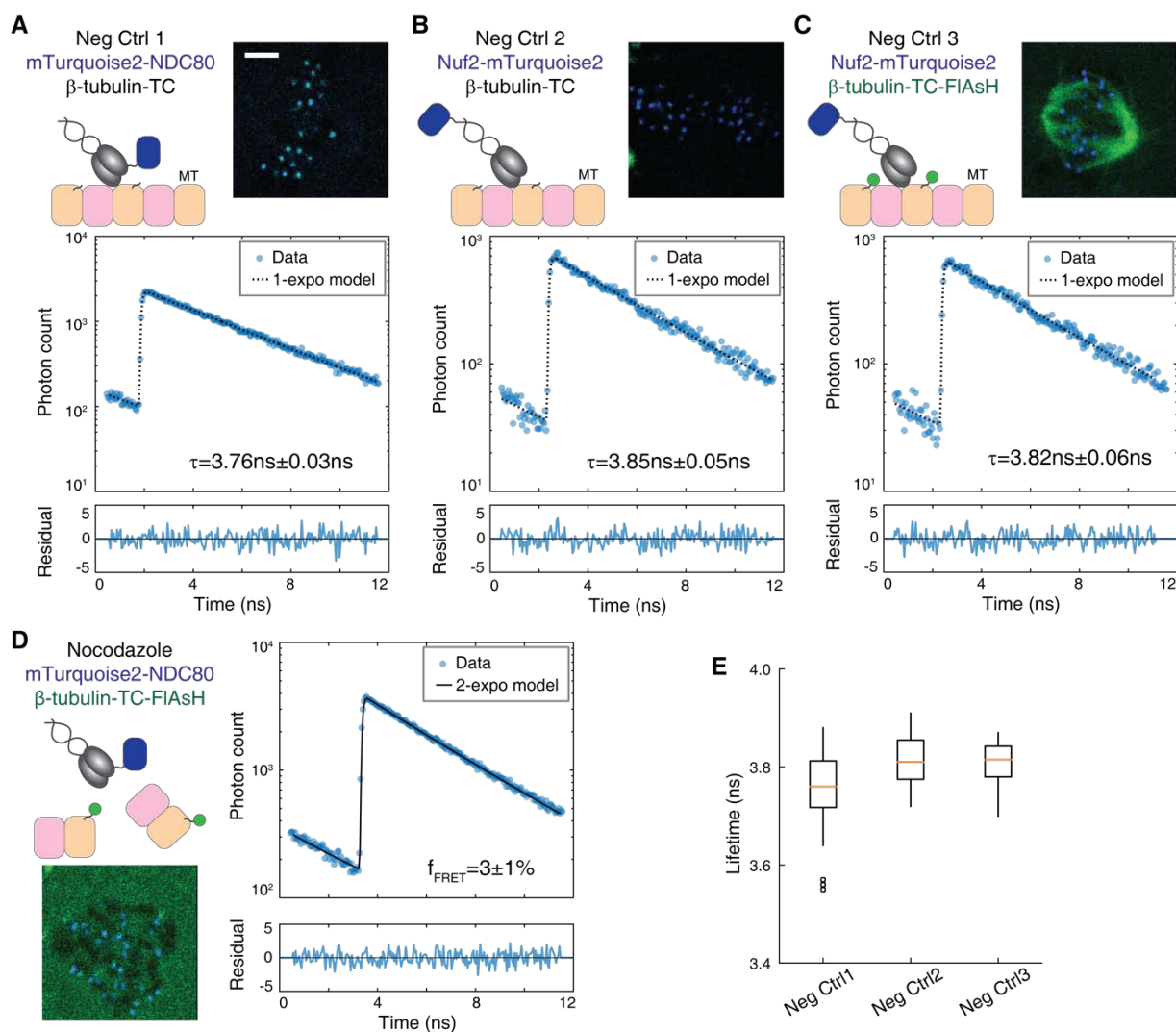


Figure S2. Negative control data for NDC80-kMT FLIM-FRET measurements

(A) to (D) Schematic descriptions, example cell images, and example mTurquoise2 fluorescence decay curves of three different FRET-negative control experiments and a nocodazole treatment experiment. mTurquoise2 fluorescence decay curves (blue circles) are plotted with best-fit single- (black dotted line) or two-exponential decay model (black solid line), and the associated weighted residuals are plotted below (blue curve). 3 μm scale bar.

(A) Negative control 1. Nuf2 N-terminally labeled with mTurquoise2, and no FIAsH labeling.

(B) Negative control 2. Nuf2 C-terminally labeled with mTurquoise2 (far from kMT), and no FIAsH labeling.

(C) Negative control 3. Nuf2 C-terminally labeled with mTurquoise2 (far from kMT), and β-tubulin C-terminally labeled with FIAsH.

(D) Nocodazole treatment experiment. Nuf2 N-terminally labeled with mTurquoise2, and β-tubulin C-terminally labeled with FIAsH. Cell was incubated with 5 μM nocodazole for >10 minutes to depolymerize microtubules.

(E) Boxplot of fluorescence lifetimes estimated from single-exponential models fit to the negative control fluorescence decays. n = 32, 11, and 6 cells for Neg Ctrl 1, 2, and 3, respectively.

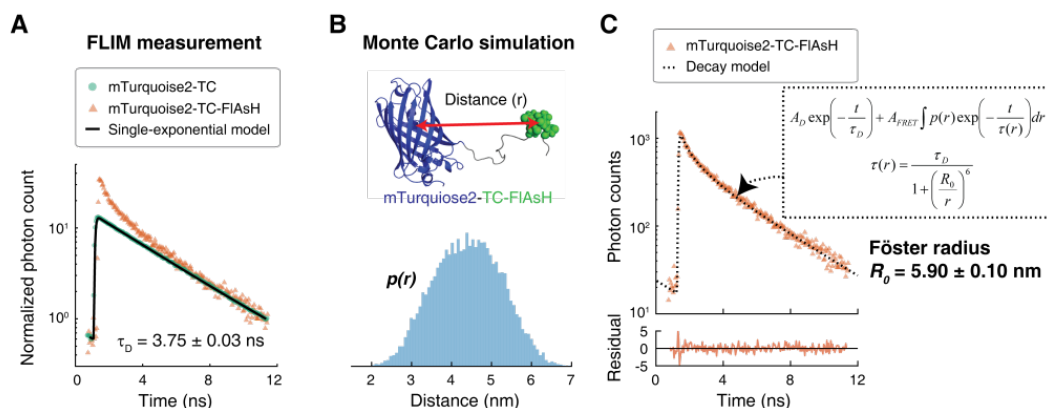


Figure S3. Förster radius estimation by FLIM-FRET measurements and Monte Carlo protein simulations

(A) Fluorescence decay curves of cells expressing mTurquoise2-TC in the absence (green circle) and the presence (orange triangle) of FIAsH. A single-exponential model (black solid line) was fit to the fluorescence decay curve in the absence of FIAsH. For visualization, the fluorescence decay curves were normalized such that they asymptotically overlap.

(B) The conformational ensemble of the flexible tether between mTurquoise2 and TC were modeled by Monte Carlo protein simulations, and the distance, r , between mTurquoise2 (blue cartoon) and TC-FIAsH (green ball) was estimated. This distribution is denoted by $p(r)$.

(C) The measured fluorescence decay of mTurquoise2-TC-FIAsH (orange triangles, same as (A) but not normalized) plotted with the best-fit decay model (black dotted line, model described in the box and Methods). Associated weighted residual plotted below. Fitting the decay model to the data estimated the Förster radius to be $5.90 \text{ nm} \pm 0.10 \text{ nm}$ (SE).

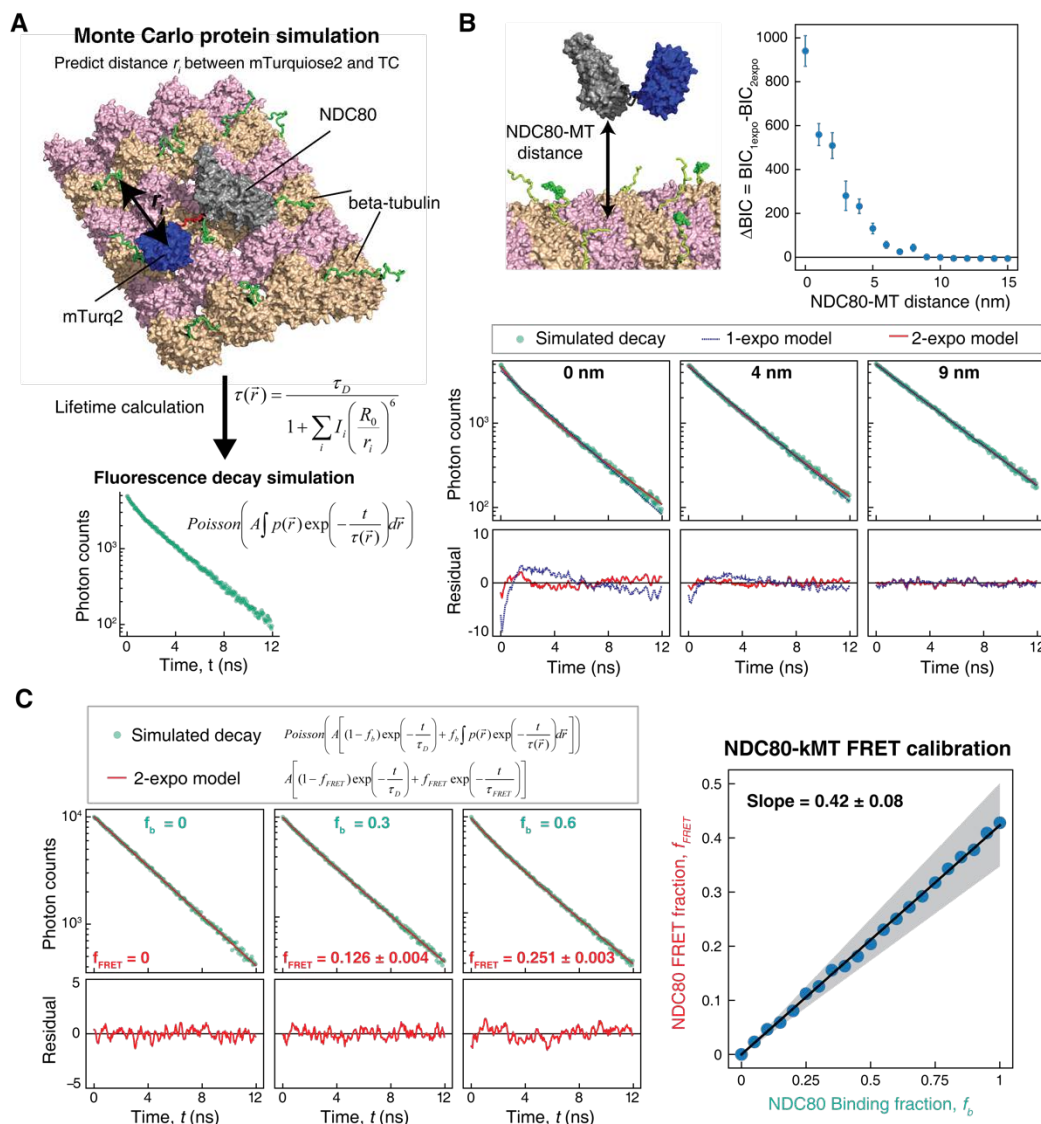


Figure S4. Characterization and calibration of NDC80-kMT FLIM-FRET measurement

(A) The conformational ensemble of the flexible tether between mTurquoise2 and Nuf2 (red) and the disordered C-terminal tails of beta-tubulins around the NDC80 (green) were modeled by large-scale Monte Carlo protein simulations, which were then used to calculate the distances, r_i , between the mTurquoise2 and the TC motifs. FAsH labeling was assigned to the TC motifs with 26.1% probability (which is the measured labeling fraction of beta-tubulin). Fluorescence lifetimes of the mTurquoise2 were calculated for randomly sampled sets of distances, $\vec{r} = \{r_i\}$, based on which fluorescence decay curves were simulated.

(B) (top) Fluorescence decay curves for various distances between NDC80 and MT were simulated and then were fit using single- and two-exponential decay models. Difference in Bayesian information criteria (BIC) between single- and double-exponential models is plotted against the NDC80-MT distance. Data points are mean and SD. (bottom) Example simulated fluorescence decay curves (green dots) for 0, 4, and 9 nm NDC80-MT distances are plotted with the best-fit single- (blue line) and two-exponential (red line) models. Corresponding smoothed weighted residuals plotted below.

(C) Fluorescence decay curves for various NDC80 binding fractions (f_b) were simulated and fit by using two-exponential decay model to estimate FRET fraction (f_{FRET}). (left) Three example simulated fluorescence decay curves (green dots) for 0%, 30%, and 60% binding fractions with the best-fit two-exponential models (red line), and the corresponding smoothed weighted residuals plotted below. (right) NDC80 FRET fractions (f_{FRET}) plotted against NDC80 binding fractions (f_b) (blue dots), and the linear fit (black line). Gray shaded area represents the uncertainty in the slope, which was determined from the uncertainties in the measured beta-tubulin labeling fraction and Förster radius (see Supplemental experiments in Methods).

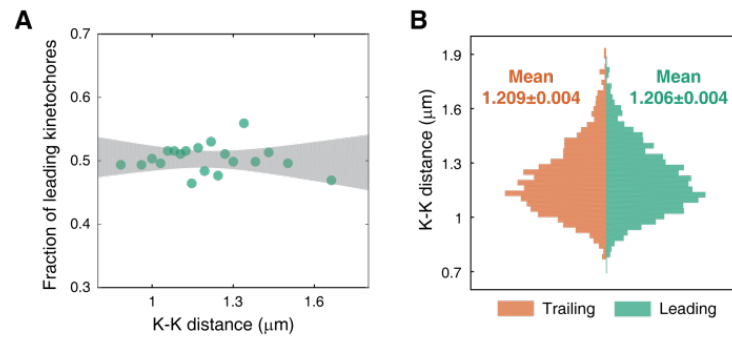


Figure S5. K-K distance and kinetochore velocity are not correlated

(A) Each data point represents the fraction of leading kinetochores within a group of kinetochores with similar K-K distances. Gray region is the 95% confidence interval of the linear fit.

(B) Histogram of K-K distances of leading (green) and trailing (orange) kinetochores.

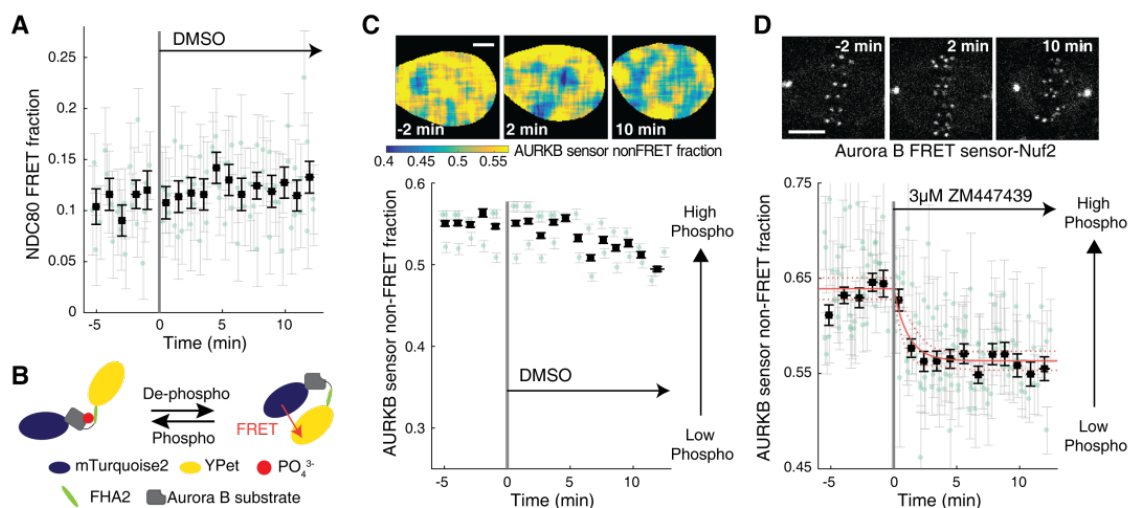


Figure S6. Supplemental data for Aurora B inhibition experiments

(A) Time course of NDC80 FRET fraction in response to 0.03% DMSO (n = 5 cells, negative control for Figure 4A).

(B) The design of Aurora B FRET biosensor. The FRET sensor contains a kinesin-13 family Aurora B substrate (gray) whose phosphorylation results in its binding to the forkhead-associated domain (FHA2, green) in the sensor, which constrains the sensor in the open non-FRET state. Therefore, measuring the non-FRET fraction of the FRET sensor allows the quantification of Aurora B activity.

(C) Time course of the non-FRET fraction of cytoplasmic Aurora B FRET sensor in response to 0.03% DMSO (n = 3 cells, negative control for Figure 4B).

(D) Time course of the non-FRET fraction of Nuf2-targeted Aurora B FRET sensor in response to 3 μ M ZM447439 (n = 9 cells). Black squares and error bars are the weighted mean and SEM of the data points (green circles) in equally spaced time intervals of 1 minute. Red solid and dashed lines are the best-fit exponential model and its 95% confidence interval, respectively. 5 μ m scale bars.

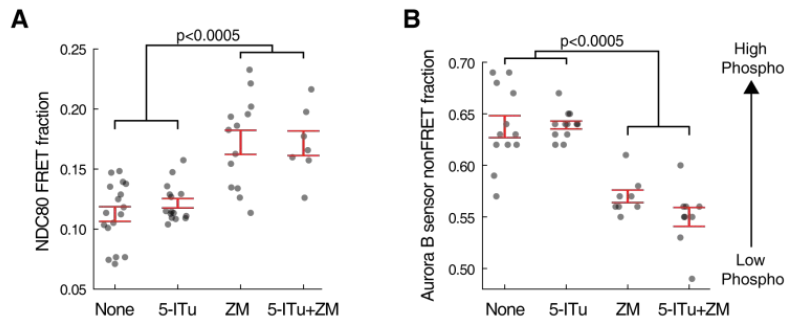


Figure S7. Displacement of haspin-dependent Aurora B from centromeres does not significantly alter the average level of NDC80-kMT binding and Aurora B activity at NDC80

(A) NDC80 FRET fraction and (B) the non-FRET fraction of Nuf2-targeted Aurora B FRET sensor (proxy for Aurora B activity at NDC80) for different drug treatments. Each data point (gray circle) corresponds to an individual cell, and the error bar (red) shows the mean and SEM. P-values from two-sided Welch's t-test.

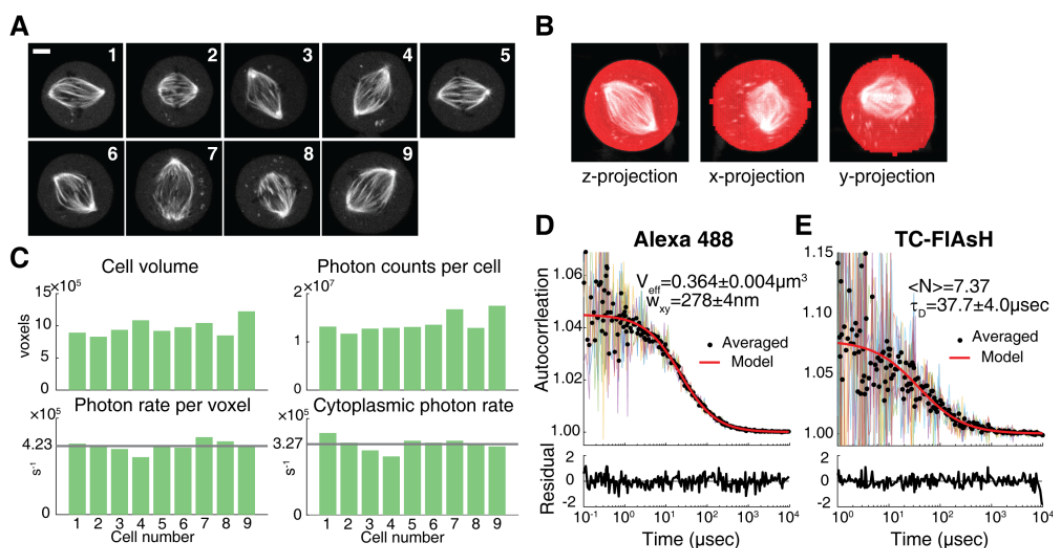


Figure S8. β -tubulin labeling fraction measurement, Related to Supplemental experiments in Methods

(A) Two-photon fluorescent microscopy images of 9 mitotic cells with β -tubulin-TC-FIAsH. 5 μm scale bar.

(B) Example 3D segmentation using active contour algorithm.

(C) (top left) The number of voxels in segmented 3D cell images, (top right) the total number of photons collected from entire cells, (bottom left) the total number of photons divided by the number of voxels and the measurement time, and (bottom right) the number of photons collected per second at a voxel in the cytoplasmic region. Gray lines are the average over the 9 different cells.

(D) and (E) FCS measurements on Alexa Fluor 488 and TC-FIAsH in solution, respectively. Black circles are averages over 5 or 6 autocorrelation functions, and red lines are a single-component FCS model fit to the averages. Corresponding weighted residuals (the difference between data and model) are plotted below.